Sub-pixel mapping of annual tree and standing deadwood cover from Sentinel-2 time series across the globe

Clemens Mosig[1], Teja Kattenborn[2], David Montero[1, 3], Janusch Vanja-Jehle[2], John Brandt[4], Nathan Jacobs[5], Subash Khanal[5], Eric Xing[5], Martin Schwartz[6], Helene C. Muller-Landau[7], Mirela Beloiu[8], Aurora Bozzini[9], Yan Cheng[10], Keenan Ganz[11], Björn Grüning[12], Henrik Hartmann[13, 14, 15], Jan Hempel[1], Stéphanie Horion[10], Samuli Junttila[16, 17], Kirill Korznikov[18], Guido Kraemer[1], Milena Mönks[1], Davide Nardi[9], Paul Neumeier[1], Jonathan Schmid[2], Salim Soltani[2], Marie Therese-Schmehl[19], Josh Veitch-Michaelis[20], and Miguel D. Mahecha[1, 3, 21, 22]

[1]Institute for Earth System Science and Remote Sensing, Leipzig University, Germany [2]Chair of Sensor-based Geoinformatics (geosense), University of Freiburg, Germany [3]German Centre for Integrative Biodiversity Research (iDiv), Leipzig, Germany [4]World Resources Institute, 10 G St NE #800, Washington, DC 20002, USA [5]Washington University in St. Louis, United States [6]Laboratoire des Sciences du Climat et de l'Environnement, LSCE/IPSL, CEA-CNRS-UVSQ, Université Paris-Saclay, France [7]Smithsonian Tropical Research Institute, Panama [8]Forest Resources Management, Institute of Terrestrial Ecosystems, Department of Environmental Systems Science, ETH Zurich, Switzerland [9]Department of Agronomy, Food, Natural Resources, Animals and Environment (DAFNAE), University of Padova, Italy [10]Department of Geosciences and Natural Resource Management, University of Copenhagen, Denmark [11]School of Environmental and Forest Sciences, University of Washington, Seattle, United States [12]Bioinformatics Group, Department of Computer Science, Albert-Ludwigs-University Freiburg, Germany [13]Institute for Forest Protection, Julius Kühn Institute (JKI) - Federal Research Centre for Cultivated Plants, Germany [14]Faculty of Forest sciences and Forest Ecology, Georg-August-University Göttingen, Germany [15]Department of Biogeochemical Processes, Max Planck Institute for Biogeochemistry, Germany [16]Department of Forest Sciences, University of Helsinki, Finland [17]Department of Remote Sensing and Photogrammetry, Finnish Geospatial Institute FGI, The National Land Survey of Finland, Finland [18]Department of functional ecology, Institute of Botany of the Czech Academy of Sciences, Třeboň, Czech Republic [19]Department of Hydrology and Climatology, Potsdam University, Germany [20]University of Florida, United States [21]Helmholtz Centre for Environmental Research (UFZ), Leipzig, Germany [22]Center for Scalable Data Analytics and Artificial Intelligence (ScaDS.AI), Leipzig, Germany

This is a preprint manuscript submitted to EarthArXiv and has not been peer reviewed.

Abstract

Elevated forest disturbances and excess tree mortality are increasingly reported worldwide. Yet existing assessments are either based on patchy terrestrial observations or on large-scale satellite products, which are limited in resolution to pixel-level, binary tree loss detection. This leaves a blind spot on fine-scale disturbances where only a few trees are declining in an otherwise intact canopy. Here, we develop and validate a model that annually retrieves sub-pixel fractional cover of standing deadwood and trees from rolling four-year windows of Sentinel-2 time series. Fractional cover is the proportion of each pixel covered by dead or live tree crowns. To obtain globally distributed sub-pixel reference labels, we leveraged the crowd-sourced archive *deadtrees.earth* of centimeter-scale drone orthophotos with two globally calibrated semantic segmentation models to derive tree and standing deadwood masks, yielding 11.1 million labeled Sentinel-2 pixels. Spatial block cross-validation yields Pearson's r = 0.64–0.68 for tree cover across biomes, and Pearson's r = 0.24–0.51 for standing deadwood cover. Evaluated on identical cells, our fractional tree cover agrees more closely with the drone reference than the Global 30 m Landsat Tree Canopy Cover and Copernicus Tree Cover Density products (weighted r = 0.73 versus 0.40 at 30 m, and 0.68 versus 0.38 at 10 m). Our method provides the missing link between fine-scale ground observations and low-resolution remote sensing products, allowing more realistic estimates of global trends in forest disturbance and tree mortality.

1 Introduction

In recent years, elevated forest disturbances and excessive tree mortality have been reported in many regions around the world (Allen et al. 2015; Hartmann et al. 2022, 2025; Senf et al. 2018; Trumbore et al. 2015). These events are the result of combined impacts due to climate change, pests, pathogens, and past forest management (International Tree Mortality Network et al. 2025). In order to better understand current and future forest dynamics, we need to advance our understanding of past mortality patterns (Migliavacca et al. 2025b). A key prerequisite for such progress is the development of spatially and temporally coherent data on tree mortality events (Hartmann et al. 2022; International Tree Mortality Network et al. 2025; Yan et al. 2024).

Field-based monitoring is the status quo for assessing global tree mortality trends, because it provides the highest accuracy at the level of individual trees. However, current monitoring networks differ strongly among and within countries in sampling design, plot size, revisit intervals (often on the order of 5–10 years), and field protocols, which limits comparability and makes it difficult to resolve year-to-year dynamics and rapid disturbance events (Hammond et al. 2022; International Tree Mortality Network et al. 2025). The access to field-inventory data is also often restricted, which limits data sharing and hampers harmonized large-scale synthesis (Hlásny et al. 2025; International Tree Mortality Network et al. 2025). As a result, the most recent global tree mortality assessment relied on synthesis efforts that compile restricted sets of field observations (Hammond et al. 2022), that are high quality but spatially severely constrained to only about 675 locations and 1303 plots globally.

Remote sensing has proven increasingly promising over the past decades for monitoring forest disturbances and tree mortality by providing observations at spatial scales that cannot be achieved with field plots (International Tree Mortality Network et al. 2025). High-resolution imagery from airplanes or drones enables direct identification of forest disturbances (Cheng et al. 2024; Schiefer et al. 2023). However, airborne and drone acquisitions are typically episodic, spatially patchy, and unevenly distributed across the globe, and therefore do not yet provide temporally continuous, standardized observations at global scale. Rather than forming a globally systematic time series, airborne and drone data are currently most useful for local or country-scale tree mortality assessments and validation data for coarser satellite-based products (≥ 10 m resolution) (Cheng et al. 2024; Junttila et al. 2024; Khatri-Chhetri et al. 2024; Schiefer et al. 2024; Schwarz et al. 2024).

Satellite-based remote sensing is well suited for global disturbance monitoring because it pro-

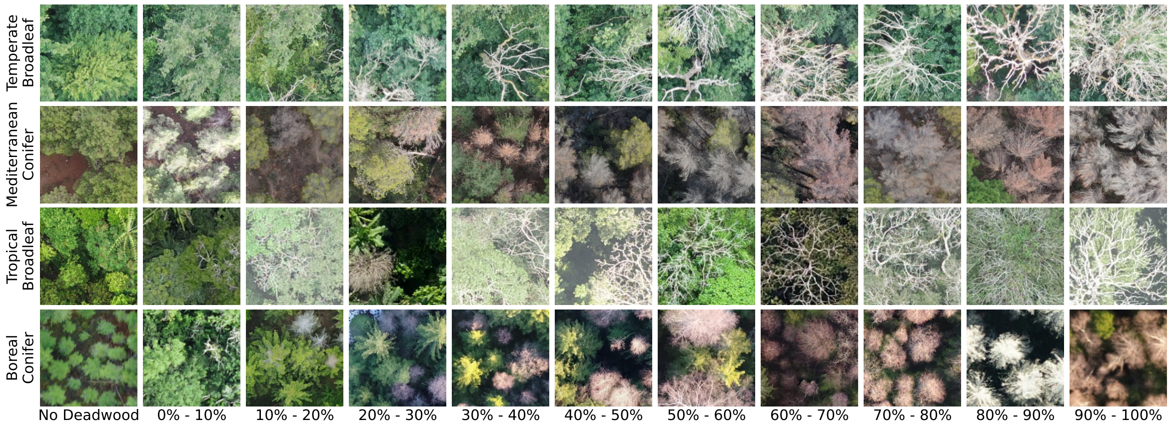

Figure 1: Drone observations of 10 $m \times 10$ m patches, the resolution that Sentinel-2 offers, with different fractions of standing deadwood cover across four major biome groups. Image data from *deadtrees.earth*.

vides spatially consistent multi-spectral images that enable systematic tracking of forest dynamics over time (Hlásny et al. 2021; International Tree Mortality Network et al. 2025). Repeat observations within seasons and across years provide valuable temporal context that helps to partially compensate for their coarse resolutions (Rußwurm and Körner 2020; Tseng et al. 2023). Several products monitor forest disturbances using Earth observation satellites (e.g., Sentinel-1, Sentinel-2, Landsat) at continental or global scales (M. C. Hansen et al. 2013; A. H. Pickens et al. 2025; Reiche et al. 2021; Senf and Seidl 2021; Song et al. 2024; van der Woude et al. 2026; Viana-Soto and Senf 2025; White et al. 2017). However, most existing products operate at spatial resolutions of ≥ 30 m and represent disturbance as a binary class (disturbed / intact), implicitly assuming within-pixel homogeneity. In reality, canopy condition and mortality are often spatially heterogeneous at sub-pixel scales, and diffuse mortality frequently affects only a fraction of the canopy within a pixel (Alix-Garcia and Millimet 2023; Hartmann et al. 2018; Korznikov et al. 2025; Schiefer et al. 2024; Y. Zhang et al. 2021, and see Figure 1). Consequently, scattered mortality and other small-scale disturbances can be missed, leading to underestimation of mortality and forest loss (Alix-Garcia and Millimet 2023; Cheng et al. 2024; Espírito-Santo et al. 2014; Schwartz et al. 2025).

Further, it is important to distinguish whether trees died standing and remain as standing deadwood (e.g., after drought stress) or whether tree cover decreased because trees were physically removed or toppled (e.g., through harvesting or wind-throw). These processes reflect different drivers and often different timing, with standing mortality frequently preceding tree loss. Separating standing deadwood from tree loss is therefore essential for robust disturbance attribution and interpretation of downstream impacts (Schiefer et al. 2023; Winter et al. 2024). Current remote sensing forest disturbance products do not disentangle such dynamics, and this imposes severe constraints on studies on tree mortality and the underlying drivers and effects on forest carbon balances and limits the development of early-warning signals (International Tree Mortality Network et al. 2025; Migliavacca et al. 2025a; Yan et al. 2024).

Explicit maps of standing deadwood over several years, in combination with fractional tree cover, are required to quantify tree mortality rates. Comprehensive real-world mortality rates are a missing component in the initialization, calibration, and validation of individual-based forest models as well as for dynamic global vegetation models (Anders et al. 2025; Bugmann et al. 2019; Hartmann et al. 2022; Sitch et al. 2008). This need for data, and especially up-to-date tree mortality maps, is exacerbated by a changing climate and thus previously unseen conditions.

Taken together, developing temporally and spatially continuous global datasets that explicitly quantify standing deadwood alongside tree cover loss is a key frontier in tree mortality research. To fill this gap, we present a methodology to retrieve *yearly fractional tree and standing deadwood cover* at 10 m resolution from Sentinel-2 time series for the years 2017 to 2025. We define *standing deadwood* as woody biomass (twigs, branches, or stems) that has died, but has largely retained its original structure, consistent with Mosig et al. 2026. The definition of *trees* includes any standing tree, dead or alive, and explicitly excludes fallen trees. We use *tree loss* for a decrease in tree cover, i.e., trees that are physically removed or have fallen (e.g., harvest, windthrow), as distinct from standing mortality, in which trees die but remain standing and thus still count as tree cover while increasing standing deadwood cover. *Fractional cover* is defined here as the proportion of a pixel that is covered by dead crowns, and enables capture of sub-pixel dynamics (Figure 1). Specifically, we aim to *(i)* estimate yearly tree and standing deadwood cover from multi-year Sentinel-2 time series at sub-pixel resolution, *(ii)* quantify model performance and generalization across biomes, and *(iii)* systematically evaluate the impact of time-series length (look-back window) on model performance. Finally, through several case studies set against ground- and expert-based observations, we illustrate how the resulting annual cover maps can be translated into forest disturbance, mortality, and recovery dynamics.

2 Methods

We developed a deep-learning model that maps Sentinel-2 reflectance time series to annual 10 m fractional tree cover and fractional standing deadwood cover, using labels derived from centimeter-scale aerial orthophotos (< 10 cm). This section is organized into two main parts: data preparation (orthophoto-derived labels, phenological alignment, and Sentinel-2 preprocessing), and model training and evaluation. Data preparation, training, and evaluation were performed at the level of 10 m $\times$ 10 m *Sentinel-2 pixels*.

2.1 Data preparation

The methodological development of globally generalizing deep learning models that map sub-pixel information on standing deadwood cover and tree cover presents three significant challenges: First, a data-driven approach resolving tree and standing deadwood cover fractions across the diversity of global forests requires ample high-quality reference data. Second, the variability of leaf-off periods in deciduous forest types across ecosystems and biomes introduces uncertainty in distinguishing deadwood from dormancy. And third, it requires availability of globally consistent remote sensing data that are temporally continuous and with a spatial resolution that allows capturing scattered mortality, i.e., at the dimensions of typical tree crowns (Fassnacht et al. 2025; Schiefer et al. 2023).

Accordingly, we assembled three core data sources that address each of those challenges. We derived georeferenced labels for standing deadwood and tree cover from drone orthophotos making use of the crowd-sourced database *deadtrees.earth* and automate the approach through deep learning segmentation models (Section 2.1.1). We determined the approximate leaf-on period for each site using remote sensing derived greenness curves (Section 2.1.2). And we acquired and preprocessed Sentinel-2 data time series in the locations where drone data is present (Section 2.1.3), Lastly, we consolidate the dataset into a high quality subset used for later training and evaluation (Section 2.1.4).

2.1.1 Orthophoto segmentation and fractional cover

We obtained masks for standing deadwood for a given orthophoto using the segmentation model by Möhring et al. 2025, which segments standing deadwood from individual branches to entire canopies. This segmentation model was trained on image resolutions ranging from 1 cm to 28 cm; however, Möhring et al. (2025) heuristically determined performance optimum at 5 cm across 434 drone or-

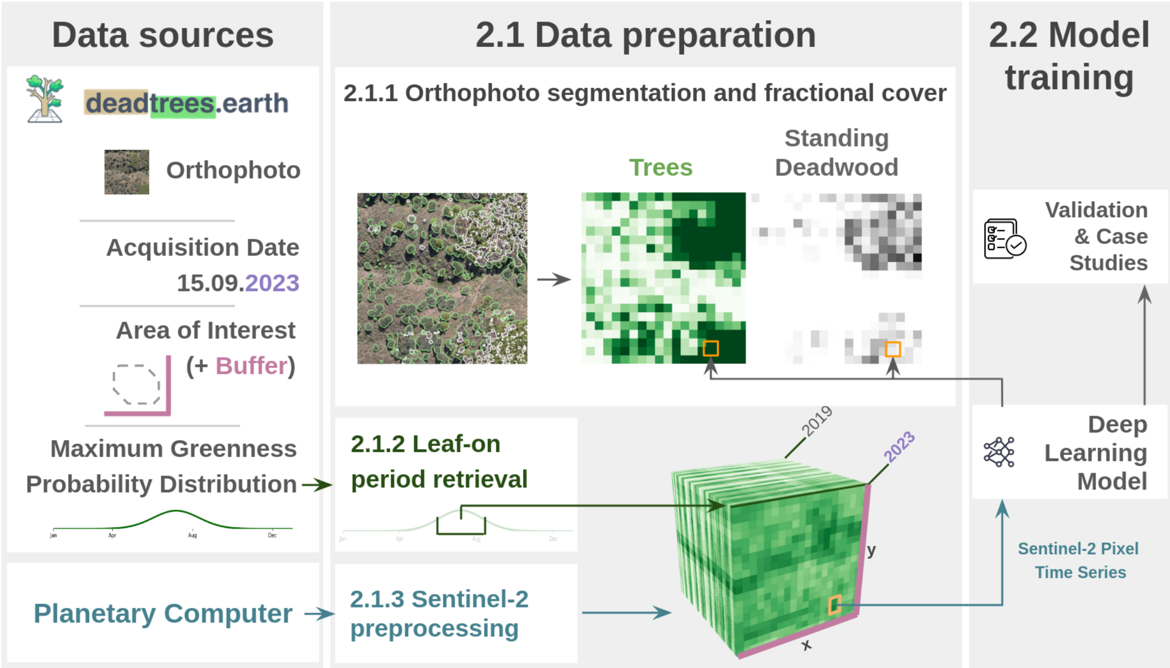

Figure 2: Data preparation flowchart for one site. Orthophotos, together with acquisition date, area of interest, and maximum greenness probability distribution, are extracted from *deadtrees.earth* (Mosig et al. 2026). Forest and standing deadwood segmentation models are applied to orthophotos, quality-checked, and then aggregated into fractional cover rasters (Möhring et al. 2025; Veitch-Michaelis et al. 2024). A season midpoint day-of-year is extracted from the maximum greenness probability distribution. The Sentinel-2 data is downloaded and preprocessed starting at the nearest season midpoint and extending 4-years into the past. Sentinel-2 cube visualization (bottom right) was created with *Lexcube* (Söchting et al. 2025).

thophotos (F1-score of 51% to 71% across biomes). Therefore, we downsampled imagery with a resolution finer than 5 *cm* to 5 *cm* with nearest neighbor reprojection before applying the segmentation model.

Tree cover masks for each orthophoto were obtained using the segmentation model by Veitch-Michaelis et al. 2024, which segments tree canopy cover, including both dead and live trees. The segmentation model achieved a mean F1-score of 91.4% in cross-validation on the OAM-TCD dataset of 541 OpenAerialMap orthophotos, of which 88 are also part of *deadtrees.earth* (Mosig et al. 2026; OpenAerialMap Community 2024). This model was trained with a fixed spatial resolution of 10 cm in the coordinate reference system (CRS) EPSG:3095. Therefore, all orthophotos were reprojected and resampled (bilinear interpolation) to match this CRS and spatial resolution before model inference. In early tests, the threshold choice for binarization (86%) showed a trade-off between either undersegmenting individual trees in sparse forests or missing canopy gaps in dense forests. Furthermore, the preliminary tests showed that this model often failed to detect standing deadwood as trees, thus we set areas as tree cover that were already segmented as standing deadwood. This ensured that standing deadwood cover is always a subset of tree cover in the reference masks. The masks of both models were visually audited and filtered before being used as reference labels (see Section 2.1.4).

For each Sentinel-2 pixel within the area of interest, we computed *tree cover* and *standing deadwood cover* based on the centimeter-scale binary segmentation masks obtained from each orthophoto. All of the above-described analysis was restricted to the area of interest. The area of interest is the high-quality area for each orthophoto, excluding regions affected by reconstruction artifacts, missing data, or inadequate illumination (e.g., deep shadow or under-/overexposure that prevented reliable visual interpretation), while retaining non-forested areas (Mosig et al. 2026).

2.1.2 Leaf-on period retrieval

Leafless but live deciduous trees cannot be robustly distinguished from standing deadwood in aerial imagery (drone, airborne, or satellite). Thus, classification of standing deadwood from such imagery requires first determining the leaf-on period, the time of year during which leafless trees are most likely dead. This leaf-on period varies geographically.

Maximum greenness periods, as derived from remote sensing data, approximately corresponds to the leaf-on season (Körner et al. 2023). The VIIRS Global Land Surface Phenology Product (X. Zhang et al. 2020) reports, at 500 m resolution and for each year between 2013 and 2022, the day-of-year of the onset and end of maximum greenness, derived from the enhanced vegetation index (EVI) (Huete et al. 2002). For each pixel and year, Mosig et al. 2026 converts the reported onset-to-end interval into a binary daily vector marking whether each day-of-year (DOY) lies within the maximum-greenness season. These vectors are then summed across all years and over 40 km cells, using only 500 m pixels with more than 50% forest cover from ESA WorldCover (Zanaga et al. 2022), yielding for each DOY a count of how often it was reported to be in season, which we use as the per-site distribution $\mathbf{y}$. We employed this probability distribution $\mathbf{y}$ to identify an estimated leaf-on season for each 40 km pixel, by defining any DOY with a probability above $(\max(\mathbf{y}) - \min(\mathbf{y}))/2$ to be in leaf-on season. If this yields multiple leaf-on seasons, we keep the longest. This estimated leaf-on season is later used to filter drone images (see Section 2.1.4) and its center used during model training and inference (see Section 2.2.1 and Supplementary Figure S1).

2.1.3 Sentinel-2 preprocessing

For each orthophoto location, we obtained a Sentinel-2 data cube (Mahecha et al. 2020; Montero et al. 2024b), with spatial bounds defined by a 100 m outer buffer around the orthophoto's area of interest in the respective UTM zone (see Figure 2). Each data cube consists of four years of historical Sentinel-2 images starting from the nearest site-specific leaf-on season center (see Section 2.1.2). For example, for an acquisition date in Sep 15th 2023, and a respective leaf-on season center in Jun 15th, the data cube extends from Jun 15th 2019 to 2023.

Data cleaning steps for optical time series have been shown to be an important step to improve model generalization capabilities (Rußwurm and Körner 2020). We unscaled the Sentinel-2 L2A digital numbers to surface reflectance by applying the radiometric offset ($-1{,}000$ for processing baseline $\geq$ 04.00) and the quantification value of 10,000 (European Space Agency 2021), and clipped the result to $[0, 1]$. To obtain a high quality time series, we retained only clear-sky observations and removed pixels affected by clouds, cloud shadow, and snow. We classified clouds and their shadows using the CloudSEN12 segmentation model (Cesar Aybar et al. 2022), applied to individual patches (732 $px \times 732$ px) with all 12 Sentinel-2 bands. Lastly, we identified and masked snow at pixel level using Fmask (v3.2) (Zhu and Woodcock 2012; Zhu et al. 2015).

Reprojection and resampling followed data cleaning. The L2A bands, acquired at 10, 20, and 60 m, were resampled to a common 10 m grid, and observations outside the local UTM zone were reprojected, both using nearest-neighbor resampling. Specifically, Sentinel-2 data is provided in a globally tiled format (Military Grid Reference System, MGRS Bauer-Marschallinger and Falkner 2023), where each tile spans 109.8 km and is stored in its local UTM zone. Due to this fixed tiling scheme across multiple coordinate reference systems, a single location can be covered by up to six separate tiles (Bauer-Marschallinger and Falkner 2023). Thus, to obtain a coherent data cube for every site, a subset of tiles was reprojected in overlapping regions. Reprojection is thus only needed where a site crosses a UTM zone boundary, and any redundant observations from such overlaps (Bauer-Marschallinger and Falkner 2023) are collapsed by the subsequent 7-day mean compositing.

The final preprocessing step consisted of the temporal composites generation, where we aggregated the spatially aligned Sentinel-2 observations into 7-day intervals by computing the per-pixel, per-band mean. Using fixed 7-day bins yields equally spaced timesteps, enabling more efficient temporal encoding schemes for deep-learning models (see Section 2.2.1). The bin width balances temporal fidelity against sequence length: narrower bins lengthen the sequence without adding observations, while wider bins average over distinct acquisitions. The number of cloud- and snow-free observations contributing to each interval varies with location and data availability; Zhou et al. (2025) report ~ 40 cloud-free Sentinel-2 observations for most regions in 2022, corresponding to on average fewer than one observation per 7-day interval. In our dataset, median cloud- and snow-free timesteps per year (after 7-day aggregation, which rarely merged observations) range from about 19 (boreal and montane) to 35 (drylands; Supplementary Figure S6). We discarded 7-day intervals without any cloud- and snow-free observations, which therefore contained no valid data.

The full processing pipeline, called *sentle*, is publicly available at github.com/cmosig/sentle.

2.1.4 Dataset filter and summary

We applied this workflow to all 8,279 orthophotos in the *deadtrees.earth* database (Mosig et al. 2026) and then filtered for three criteria. First, we filtered for orthophotos within the temporal scope 2017-2025. Second, during a qualitative audit, we excluded orthophotos where tree or standing deadwood segmentation masks (see Section 2.1.1) were incorrect or missing for approximately more than one quarter of the area of interest. Third, we excluded orthophotos that were outside the above-described local leaf-on season (see Section 2.1.2). For orthophotos with evergreen vegetation only, seasonality does not matter for standing deadwood segmentation, and can still be used as a reliable reference. Therefore, in temperate, boreal, and dryland biomes (Olson et al. 2001), local experts selected additional orthophotos based on the visually estimated genus, acquisition date, and historical Google Earth imagery. This yielded 3,948 orthophoto sites and 11.1 million derived Sentinel-2 pixels (110,682-hectare) for training and validation (Figure 3; for the cover value distribution see Supplementary Figure S7).

Biome separation is based on (Olson et al. 2001), and consists of boreal and montane, dryland, temperate and (sub) tropical forests.

2.2 Model training and evaluation

2.2.1 Model Definition

We trained a per-pixel model that maps a Sentinel-2 reflectance time series (12 bands per 10 m pixel) to tree and standing deadwood fractional cover. The reflectance time series starts at the center of the

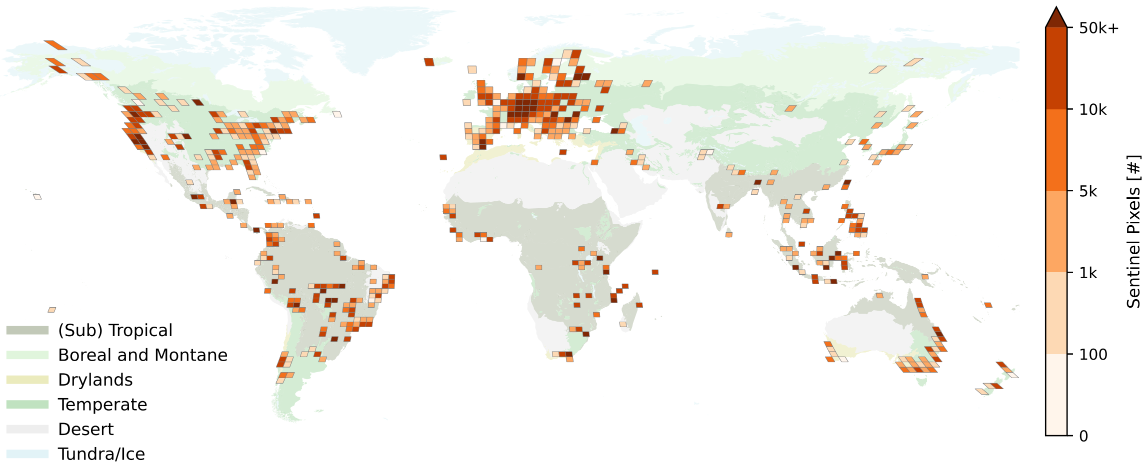

Figure 3: Global distribution of available reference data. The color indicates the number of labeled Sentinel-2 pixels within the respective 200 km bin. The spatial bins are created in EPSG:8857, an equal area projection. Different colors in the background depict different biomes (Olson et al. 2001).

nearest leaf-on period relative the orthophoto acquisition date, and each timestep represents a 7-day composite (see Section 2.1.3). The covered timespan is set to least 4 weeks and at most 4 years, and depends on data availability; Sentinel-2 is available from mid-2015 such that for predictions in 2017 the time series will only cover 2-years. At a temporal resolution of one aggregated timestep per 7 days, this corresponds to between 4 and 208 timesteps, depending on the number of cloud-free and snow free observations.

The model independently embeds each timestep: a two-layer ReLU feed-forward network with batch normalization (Ioffe and Szegedy 2015; Nair and Hinton 2010) maps the 12-band input to 2048 units and then down to a 128-dimensional embedding. It then adds sinusoidal positional encodings tailored to the temporal sequence (indexed by 7-day intervals) to reflect the temporal order and missing timesteps (Tseng et al. 2023; Yuan et al. 2022). The encoded sequence with a prepended classification token (CLS) is passed into a transformer with two encoder layers, a single self-attention head, embeddings size 128, and a 512-wide feed-forward sub-layer. Variable length sequences, e.g. through data availability and cloud cover, are enabled by a key padding mask. The previously inserted CLS token is then extracted from the transformer output and passed into a linear projection that maps the token (size 128) to the two target fractional cover values.

2.2.2 Loss function and weighting

We employed a distributional histogram loss, HL-Gauss, where regression values are represented as a categorical distribution, which was shown to consistently outperform standard regression loss functions in related work (Farebrother et al. 2024; Imani and White 2018; Imani et al. 2024). We chose 50 bins (2% cover bin width) for the loss formulation, at which performance was shown to converge (Imani and White 2018; Imani et al. 2024). The conversion from a regression target y to a categorical distribution uses a Gaussian distribution as follows:

$$P(b_i|y_p,\sigma_p) = \frac{\Phi\left(\frac{u_i - y_p}{\sigma_p}\right) - \Phi\left(\frac{l_i - y_p}{\sigma_p}\right)}{\Phi\left(\frac{u_{max} - y_p}{\sigma_p}\right) - \Phi\left(\frac{l_{min} - y_p}{\sigma_p}\right)} \tag{1}$$

where p is the pixel identifier, y_p is the target fractional cover, b_i is the i-th bin, l_i and u_i are the lower and upper bounds of bin i, $\Phi(\cdot)$ is the standard normal Cumulative Distribution Function (CDF), l_{min} and u_{max} are the bounds of the extended support (with 10 extra bins), and σ_p is pixel-specific standard deviation. We add support outside the valid value range totaling 70 bins, as it is important to enable the model to predict exactly 0% as a pixel can contain exactly no standing deadwood or no forest, which becomes especially relevant when providing statistics over large areas. Different from Imani and White 2018, σ_p is computed dynamically from the fractional cover of neighboring pixels to represent georeferencing uncertainty (see Section 5.3):

$$\sigma_p = \mathrm{std}(\{y_o : o \in \mathcal{N}(p)\}) \tag{2}$$

where $\mathcal{N}(p)$ is the neighborhood around pixel p containing the set of identifiers of directly adjacent pixels.

Lastly, given the naturally long-tailed distribution of fractional cover we applied the inverse frequency of cover value ranges as weight to the loss. We used coarser 20% bins, different from the above 2% bins, for increased weight stability with small sample sizes. Specifically, the loss weight for each target value y is computed as: $w(y) = \frac{1}{f(g(y))}$, where $g(y) = \lfloor y/0.2 \rfloor$ maps the fractional cover value to its corresponding 20% bin and f computes the batch-wise frequency of a 20% bin.

The final HL-Gauss loss function is:

$$\mathscr{L}_{HL-Gauss} = \frac{1}{|B|} \sum_{p \in B} w(y_p) \cdot \text{CrossEntropy}(z_p, P(\cdot|y_p, \sigma_p)) \tag{3}$$

where B is the batch and z_p are the predicted logits.

To convert the categorical distribution back to a regression value, we apply a softmax to obtain bin probabilities and then compute the dot product of these probabilities with the bin-center vector; the resulting expectation is clipped to the range 0%–100%.

$$\hat{y} = \text{clip}\left(\sum_{i=1}^{N} \text{softmax}(z_i) \cdot c_i, 0, 1\right) \tag{4}$$

where z_i are the model logits for bin i, $c_i = \frac{l_i + u_i}{2}$ is the center of bin i, and N is the total number of bins (60 bins: 50 main bins plus 10 padding bins).

Because the model predicts a full categorical distribution over ordered bins, we can derive a distributional spread (standard deviation) in the original regression space, which can be used as an uncertainty indicator. We computed standard deviation from the categorical distribution is computed as:

$$\hat{\sigma} = \sqrt{\sum_{i=1}^{N} \text{softmax}(z_i) \cdot (c_i - \hat{y})^2} \tag{5}$$

2.2.3 Hyperparameters

We train with AdamW (Loshchilov and Hutter 2019) at a base learning rate of 5×10^{-6} and weight decay 0.1, applied only to weights while excluding biases, normalization parameters, positional encodings, and the CLS token. The schedule warms up linearly for the first 100 update steps from 1×10^{-7} to 5×10^{-6}, then follows a single-cycle cosine annealing decay over the remaining steps of the 200 training epochs. No early stopping was applied. Batch size is 512. Dropout is 0.2 in both the token embedding stage and the transformer layers, and we additionally apply timestamp dropout with probability 0.1.

2.2.4 Data augmentation

We employ several data augmentation techniques to reflect real-world uncertainties and data variability. For Sentinel-2 time series, we crop to a random temporal context length between four weeks and four years, ensuring stable inference for 2017–2018, where far less than four years of spectral history is available. To mimic cloudier conditions, 10% of timesteps are randomly dropped. Reflectance values are shifted by a random gain factor drawn from a normal distribution ($\mu = 0$, $\sigma = 0.03$), consistent with reported Sentinel-2 calibration results ((ESA) 2023, December 11). The extracted peak-season day of year is shifted by a random number of days sampled from $\mathcal{N}(0, 7\text{d})$, and target fractional cover values are jittered with $\mathcal{N}(0, 0.1)$.

2.2.5 Epoch sampling and geographical stratification

The dataset employed here required careful balancing before model training to account for differing geographic and standing deadwood distributions. We therefore employed a geographic stratification that limits how much any single site or region can contribute to model training and evaluation. First, the crowd-sourced drone data are unevenly distributed across the globe (Figure 3), reflecting independent collection decisions by database contributors. Second, there is wide variation in the size of the area that a single orthophoto covers, and thus also in the available labeled Sentinel-2 pixels. For example, the 100 km $\times$ 100 km area with the most data represented 4% of the total data set (248,000 Sentinel-2 pixels). Additionally, the largest orthophoto (122,000 Sentinel-2 pixels) covers three orders of magnitude more area than the median (120 Sentinel-2 pixels).

Because of this, we limited the number of Sentinel-2 pixels that a single site and region can contribute to each training epoch to a fixed Sentinel-2 pixel count determined as follows: We first split the Sentinel-2 pixels into two groups: those with 0% deadwood cover and those with $> 0\%$ deadwood cover, enabling us to reduce the representation of non-deadwood pixels in the training dataset. Then, for both splits, we limited the number of Sentinel-2 pixels sampled per orthophoto to 100 (1 ha). Additionally, we reduced geographic imbalances in the data by sampling a maximum of 500 Sentinel-2 pixels (5 ha) per global grid cell of $10,000\ km^2$. Instead of applying these caps once, we decided to resample during training with these caps from the full dataset in every epoch. Across epochs, samples for $> 0\%$ standing deadwood cover remain largely the same as they are scarce, and samples for $= 0\%$ standing deadwood cover will vary across epochs. This naturally regularizes the model training, while keeping the distribution balanced and geographically representative. The outer-folds for evaluation were subsampled once with this methodology.

2.2.6 Evaluation

To avoid optimistic model performance estimates due to spatial autocorrelation, we employ spatial block cross-validation (Kattenborn et al. 2022; Ploton et al. 2020). We divide the dataset into 50 km spatial blocks in the equal-area coordinate reference system EPSG:8857 and randomly assign blocks to ten outer folds. Within each outer fold, 10% of blocks are held out as a validation split during hyperparameter tuning. Results are reported across the concatenated outer-fold test sets, and variability across folds is expressed as either standard deviation or minimum and maximum.

First, as a regression task, we evaluated recovery of tree cover and standing deadwood cover by computing Pearson's correlation coefficient (r) and the root mean square error (RMSE) for each cover type. To reduce the influence of the strongly imbalanced label distribution, we report *bin-resampled* estimates for these metrics: we partitioned the reference cover into 0.1-wide bins over $[0,1]$ and assigned each sample a weight inversely proportional to the number of samples in its corresponding label bin (computed per cross-validation fold), such that each label bin contributes equally within a fold. Weighted r and weighted RMSE were then computed independently for each fold and summarized as mean and standard deviation across folds. In addition, we report the mean error (ME) as the unweighted mean of $(\hat{y} - y)$ computed over all pixels within each biome, to reflect the average bias under the natural data distribution.

Second, we evaluated the predictions as a binary classification task. Viewing the problem additionally as a binary classification task is important in the context of scattered mortality (or individual trees), where uncovering the presence/absence of a (dead) tree is much more important than getting the exact fractional cover value (see Section 5.3). Here, we binarized tree cover and standing deadwood cover at a threshold of 0%: any non-zero cover counts as present. We then computed precision (complement of the commission error) for the present cover class over each predicted fractional range of 5%, and, conversely, recall (complement of the omission error) over each target fractional range of 5%. For recall, a pixel is counted as detected when its predicted cover exceeds a detection threshold. We only considered 5% bins with more than 20 observations for result stability. This means that a recall of 50% at a *target* fractional cover value of 20% corresponds to the model predicting cover above the detection threshold in 50% of cases where the cover is 20%. Conversely, a precision of 50% at a *predicted* cover value of 20% corresponds to the model being right in 50% cases that cover is present ($> 0\%$). Practically, precision can be interpreted as the probability that a location with a given predicted deadwood cover indeed contains at least one (dead) tree. And recall indicates the share of pixels with a certain fractional cover that the model predicts as any standing deadwood.

2.3 Temporal context experiment

To quantify the value of increasing historical reflectance context, we evaluated model performance as a function of the input time-series *timespan*, defined as the duration between the first and last timestamp, irrespective of the number of cloud-free observations within that interval. For each trained model, we passed all samples from the cross-validation splits through the network and recorded predictions for progressively cropped timespans between 16 and 192 weeks in 16-week increments, and for the 4-week timespan as an additional minimum-context setting. To ensure comparability across timespans, we used only samples with valid predictions for all evaluated durations and in that process aggregated to 16-week bins to maintain sufficient coverage in regions with comparatively few cloud-free observations (see Supplementary Figure S6). The minimum evaluated timespan of 4 weeks corresponds to the shortest temporal context encountered during training via data augmentation (see Section 2.2.4). Performance was assessed using two complementary metrics: weighted Pearson's correlation coefficient (r) to evaluate recovery of fractional cover in the regression setting, and the F1-score computed from mean precision and recall across 5% fractional-cover bins for the binary classification task, consistent with the general evaluation protocol (see Section 2.2.6).

3 Results

This section reports cross-validation binary classification and fractional cover regression performance across biomes (Section 3.1 and Section 3.2). We further investigate how model performance responds to increasing lengths of historical Sentinel-2 time series, thereby quantifying the value of temporal context for tree cover and standing deadwood cover mapping (Section 3.3).

3.1 Classification performance

We evaluated the predictions as a binary presence/absence classification (threshold 0%; see Section 2.2.6). Because at a 0% threshold almost any prediction is non-zero and recall would be near-uninformative, we report recall for an exemplary detection threshold of 10%, and for the stricter thresholds of 20% and 30% in Section A.8. For tree cover, both precision and recall increased with

Table 1: Mean and standard deviation (across cross-validation folds) of bin-resampled weighted Pearson's r and RMSE, and unresampled mean error (ME), for tree and standing deadwood cover.

Biome	Metric	Tree	Standing Deadwood
(Sub) Tropical	Pearson	0.64 (0.04)	0.41 (0.17)
	RMSE	0.26 (0.02)	0.45 (0.05)
	ME	-0.05 (0.02)	0.03 (0.01)
Boreal and Montane	Pearson	0.64 (0.04)	0.24 (0.27)
	RMSE	0.25 (0.02)	0.39 (0.09)
	ME	-0.07 (0.03)	0.03 (0.02)
Drylands	Pearson	0.68 (0.03)	0.35 (0.22)
	RMSE	0.25 (0.02)	0.42 (0.07)
	ME	-0.06 (0.04)	0.04 (0.01)
Temperate	Pearson	0.67 (0.02)	0.51 (0.13)
	RMSE	0.24 (0.01)	0.36 (0.05)
	ME	-0.05 (0.02)	0.05 (0.01)

fractional cover, approaching one above roughly 50% cover (Figure 4a): high fractional tree cover predictions were increasingly likely to contain a tree pixel (precision), and higher target tree cover was increasingly likely to be detected (recall). At low tree cover, precision was highest in drylands, while recall was highest in temperate and boreal forests.

For standing deadwood cover, precision and recall were lower and more variable across biomes (Figure 4b). Recall increased with target standing deadwood cover in all biomes and was highest in temperate and lowest in (sub) tropical forests. Precision increased with predicted standing deadwood cover but remained below 0.5 for boreal and (sub) tropical forests, whereas in temperate forests it reached close to one at high predicted standing deadwood cover.

3.2 Sub-pixel fractional cover estimation performance

The following results compare predicted and target fractional cover. For tree cover, regression performance was stable across biomes, $r = 0.64 - 0.68$ and $\text{RMSE} = 0.24 - 0.26$, with very small fold-to-fold variability ($\sigma_r = 0.02 - 0.04$ and $\sigma_{\text{RMSE}} = 0.01 - 0.02$), indicating consistent performance across folds. Tree cover showed consistent underestimation ($\text{ME} = (-0.05) - (-0.07)$) compared the drone derived masks.

In contrast, standing deadwood cover showed a stronger biome dependence. The highest correlation was obtained in temperate forests ($r = 0.51$, $\text{RMSE} = 0.36$). RMSE fold-to-fold variation was lowest for temperate and (sub) tropical forests ($\sigma_{\text{RMSE}} = 0.05$) and highest for boreal and

(a) Precision and recall for fractional tree cover.

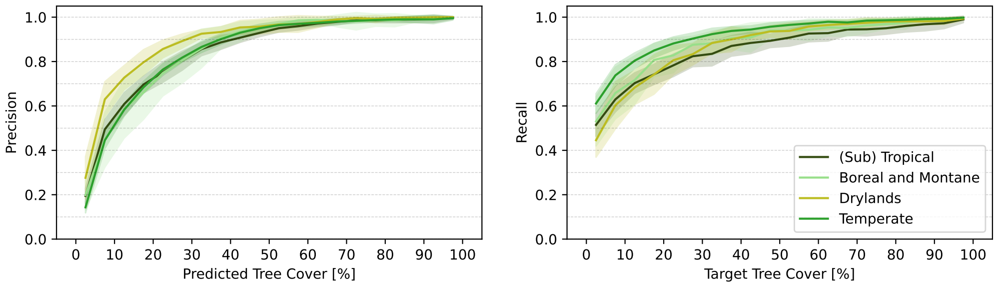

(b) Precision and recall for fractional deadwood cover.

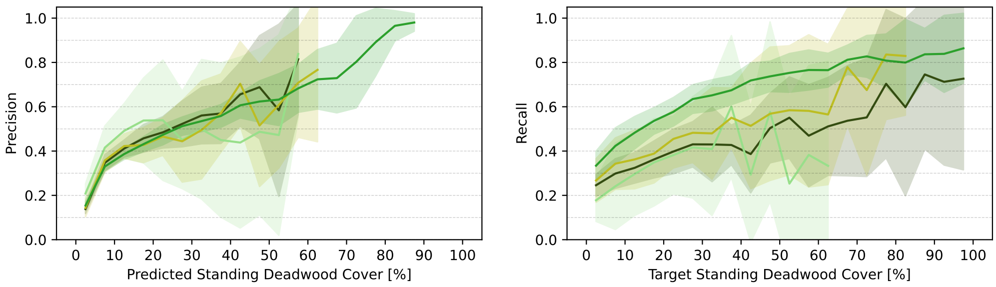

Figure 4: Mean precision and recall in the binary performance task across fractional cover bins (width = 5%). For the precision, the x-axis represents the predicted fractional cover (left). For the recall, the x-axis represents the target fractional cover (right). The recall panels use an exemplary detection threshold of 10%. The shaded band denotes one standard deviation across the ten cross-validation folds. Only results for 5% bins with more than 20 samples are displayed.

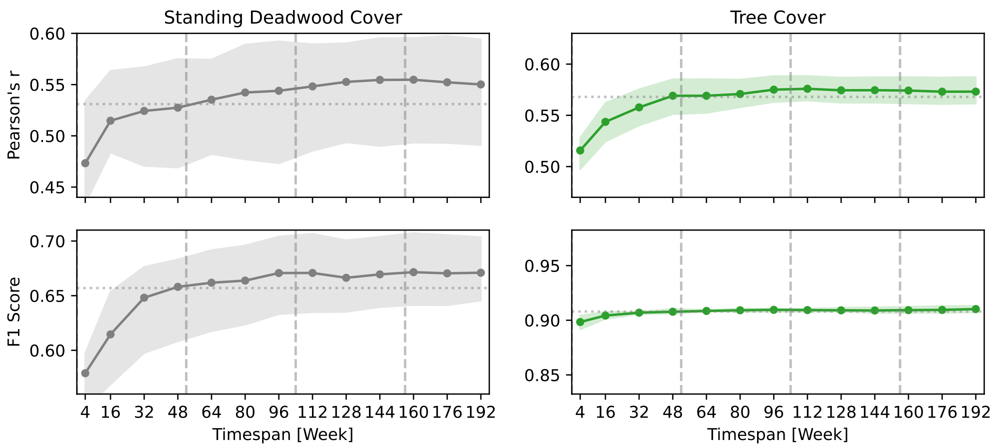

Figure 5: Mean model performance across folds and the covered timespan. F1-score measures binary classification of Sentinel-2 pixels and Pearson's r exact fractional cover retrieval. The displayed range in the y-dimension denotes the minimum and maximum performance across folds. The extent on the y-axis has the same height between standing deadwood cover and tree cover for the same metrics to enable comparison. Vertical dashed lines are drawn at year boundaries. A horizontal dotted line is drawn at the respective performance with one year of temporal context.

dryland forests ($\sigma_{\text{RMSE}} = 0.07 - 0.09$). Standing deadwood was consistently overestimated (ME $=$ $0.03 - 0.05$) compared to drone derived masks.

Overall, fold-to-fold variation was lower for tree cover than for standing deadwood cover. Performance was also consistently higher for tree cover. Scatter plots comparing predicted and reference cover values can be found in Section A.7.

3.3 Performance impact of time series length

Overall, performance increased with longer input timespans (see Figure 5). This improvement was primarily driven by substantial gains within the first year (52 weeks) of historical context. Extending the time series beyond one year further improved standing deadwood classification performance (F1-score) up to approximately two years and enhanced standing deadwood cover regression performance (Pearson's r) up to approximately three years. In contrast, tree cover regression showed only marginal gains beyond one year, while tree cover classification largely converged after 32 weeks. Variability across cross-validation folds was greater for standing deadwood cover than for tree cover, yet the overall trend of increasing performance with longer timespans remained consistent.

3.4 Qualitative comparison against drone orthophotos

Qualitative comparison of predicted against reference cover for individual held-out sites shows that spatial patterns of tree cover are recovered consistently (Figure 6). Where the reference saturates at 100% cover, the model instead retains variability that appears better aligned with the open canopies visible in the drone orthophotos. For standing deadwood, the model recovers the spatial pattern of mortality but frequently not its exact fractional cover. This also holds in drylands, where herbaceous ground cover contributes substantially to the pixel time series (sites 5791 and 350 in Figure 6). Predictions are generally smoother than the reference, so individual pixels of high reference cover are attenuated. False positives occur predominantly at low fractional deadwood cover, and low-cover patterns that trace real mortality at some sites correspond to no reference deadwood at others (Figure 7). At some sites these patterns follow the forest edge (sites 210 and 4652), and at one tropical site (7480) the model indicates considerably more mortality than the reference contains.

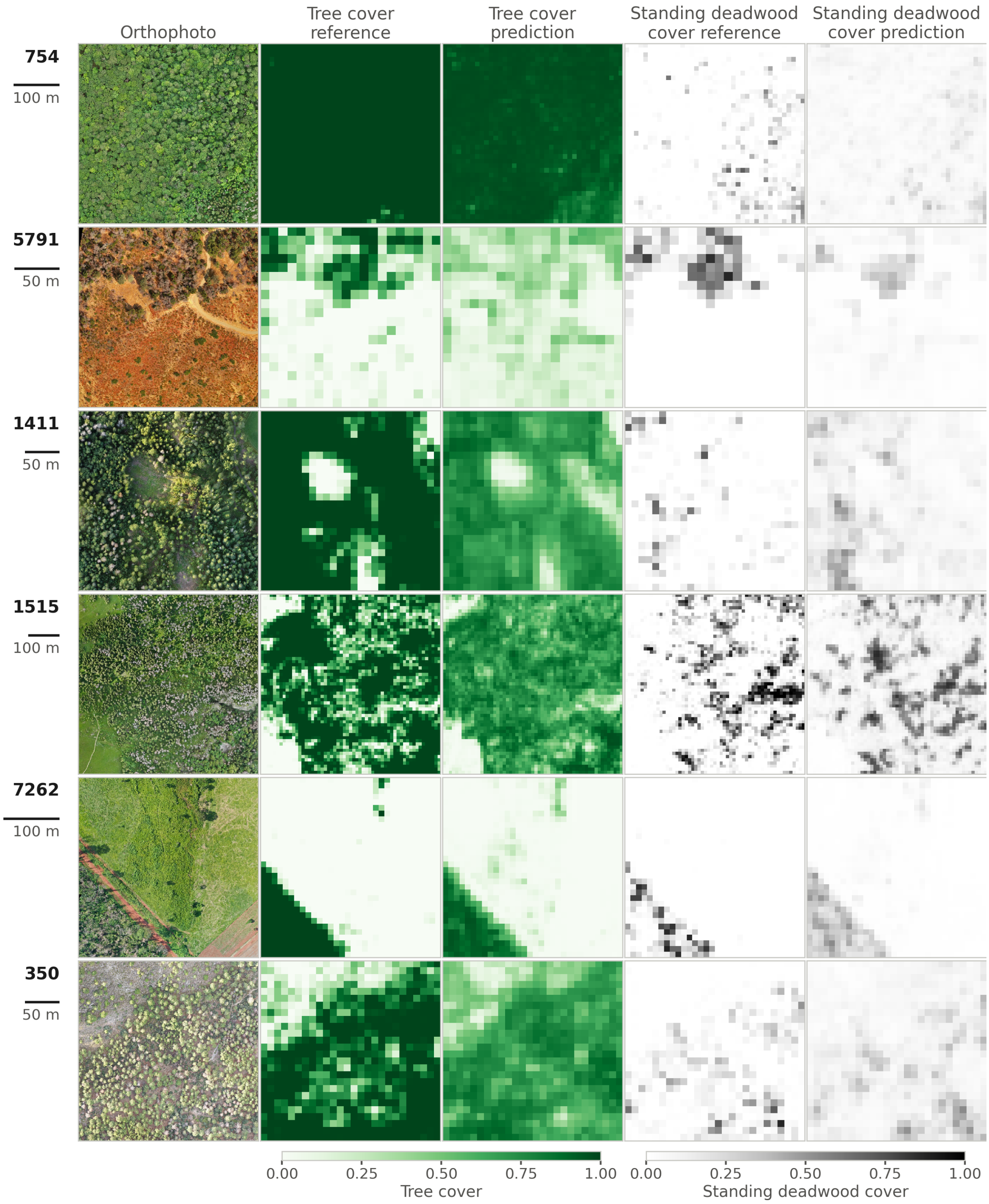

Figure 6: Reference and predicted fractional cover for a diverse set of six representative, well-performing held-out sites. Columns from left to right: drone orthophoto, tree cover reference derived from that orthophoto, tree cover prediction, standing deadwood cover reference, and standing deadwood cover prediction. The number to the left of each row is the *deadtrees.earth* dataset identifier, accessible at deadtrees.earth/dataset/⟨ID⟩.

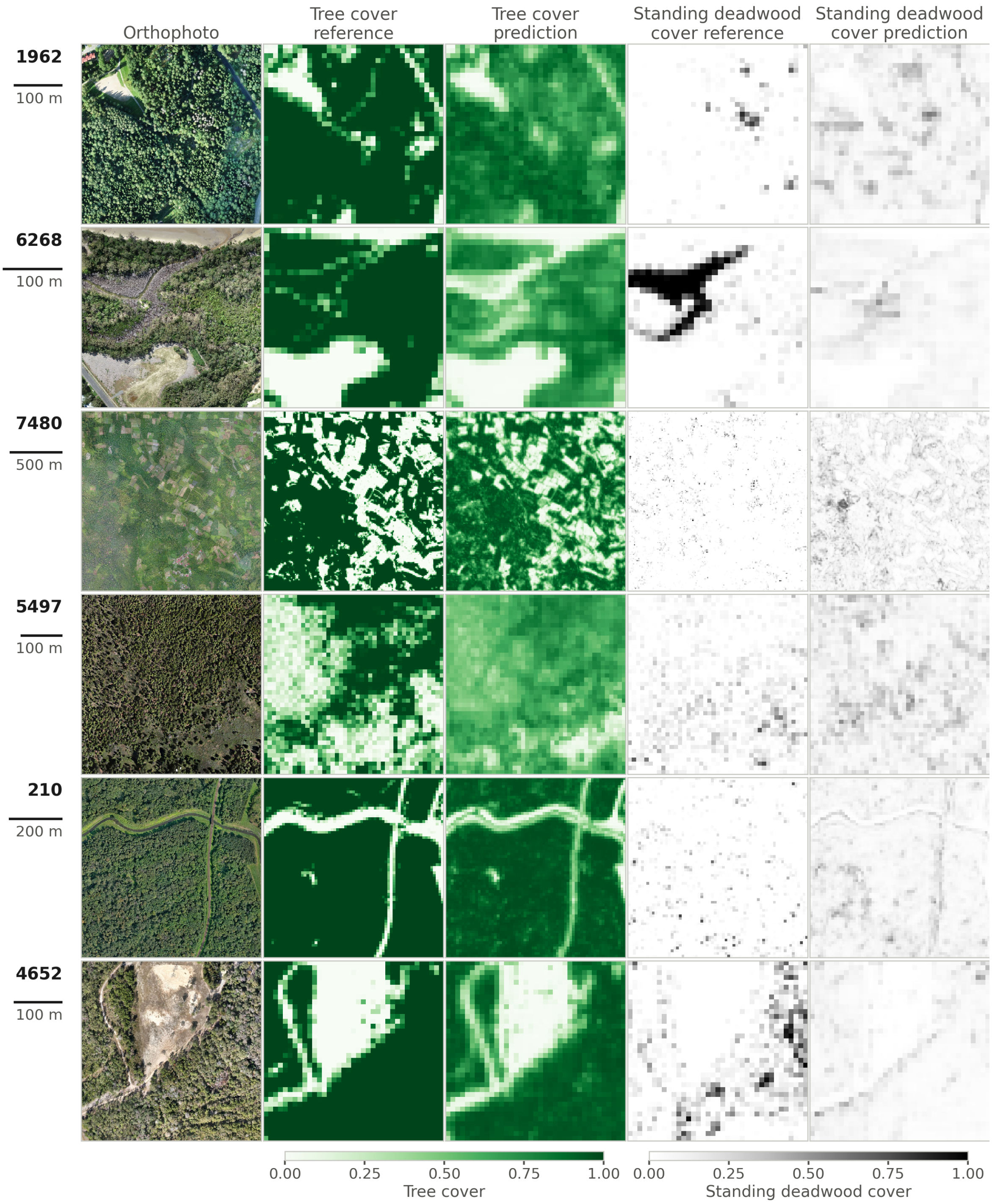

Figure 7: As Figure 6, but for six held-out sites selected specifically to illustrate the model's modes of failure.

4 Case studies: translating cover maps into disturbance dynamics

While the model is trained to estimate tree and standing deadwood cover for the acquisition year of each orthophoto, applying it to every year of the Sentinel-2 archive yields annual cover time series. These time series expose the temporal dimension of forest change that the year-matched drone comparisons in Section 3 cannot capture. We present three case studies that demonstrate how the annual cover maps can be translated into application-oriented monitoring products: recovering the year of forest loss, monitoring post-disturbance recovery, and mapping the timing of tree mortality. For each case study, the maps were generated with custom models where all orthophoto sites within 10 km (if present) of the respective case study were excluded during training.

4.1 Case study 1: mapping the year of tropical forest loss (Northern Brazil)

Tropical forests are being altered rapidly, and monitoring forest loss is essential because it is tightly linked to biodiversity decline, carbon emissions, and cascading impacts on ecosystem services and local livelihoods. As a first application pathway, we translate the annual tree cover maps into the year of forest loss, as commonly provided by dedicated disturbance products (M. C. Hansen et al. 2013; Reiche et al. 2021; Vancutsem et al. 2021). For a region in the central Amazon with evidence of small-scale logging (Figure 8), we computed for every pixel the first year in which mapped tree cover dropped below 50%, yielding a year-of-loss map that delineates deforestation patches with sharp boundaries matching the high-resolution reference image. Because the model maps fractional tree cover year over year, the same time series also reveals post-disturbance regrowth, which is highly heterogeneous after tropical logging: the bottom-left patch, lost between 2019 and 2020, has regained tree cover in the June 2024 map, consistent with the high-resolution reference.

Comparing the same area against three established products shows what the annual cover time series adds (Figure 8). Global Forest Watch (M. C. Hansen et al. 2013) and the Tropical Moist Forest product (Bourgoin et al. 2024; Vancutsem et al. 2021) captured the larger clearings but merged adjacent patches and omitted the smallest openings, while much of the affected area lies outside the RADD forest baseline (Reiche et al. 2021), so no alerts can be issued there irrespective of detection performance. The products further differ in how many events they can represent: Global Forest Watch records a single loss year per pixel, so much of what we date to 2019 or later falls within areas it already recorded as lost before 2019, where renewed clearing goes unregistered, whereas the Tropical Moist Forest product resolves recurrent disruptions. Mapping the state of tree cover in each year imposes no such limit, so successive losses and the recovery between them remain visible in the same series. Both properties matter on logging frontiers, where small openings precede full clearing and the recovery that follows is equally gradual, so neither the onset nor the aftermath of deforestation is resolved by binary disturbance products.

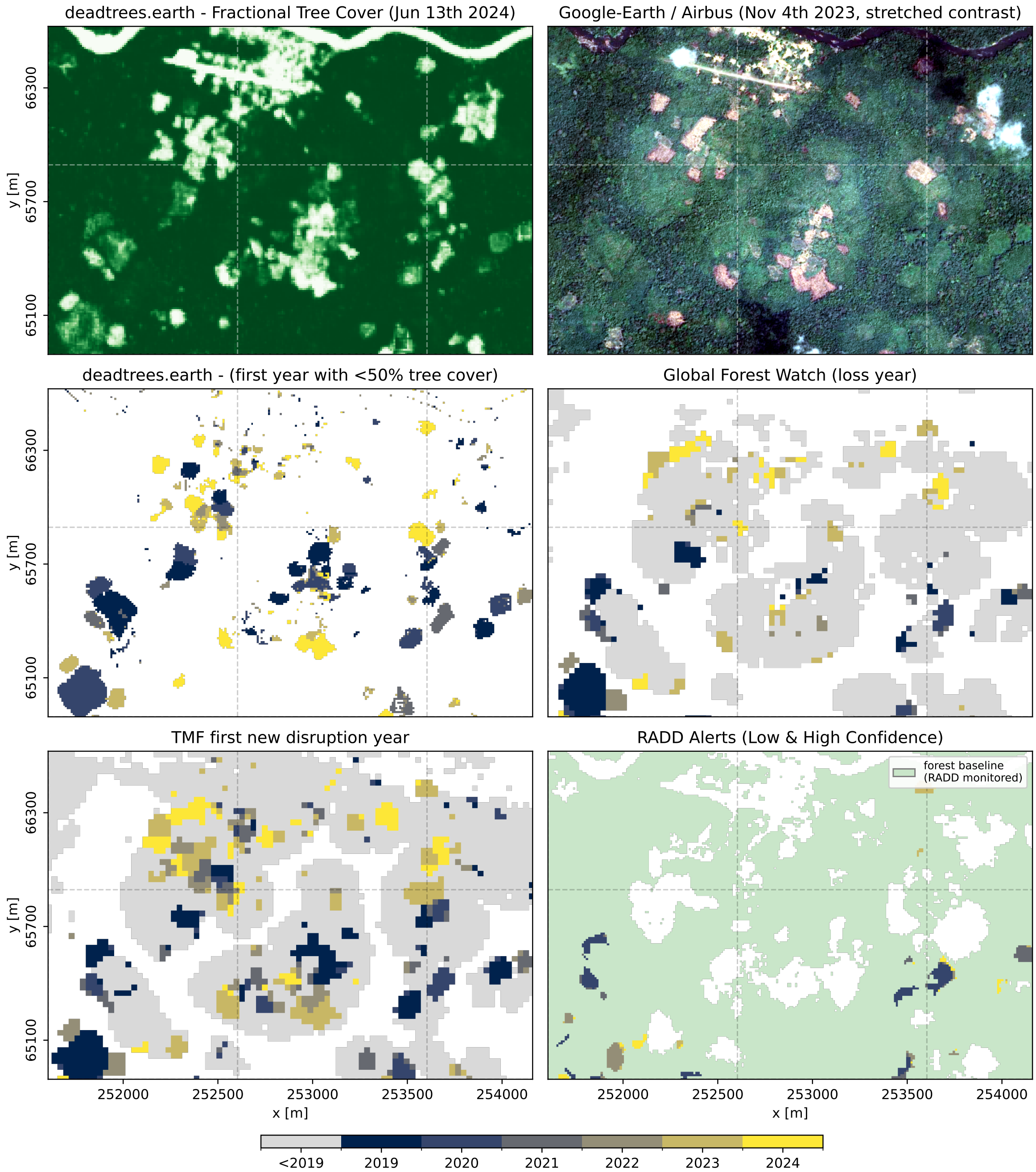

Figure 8: Comparison of disturbance timing and spatial detail across independent forest-change products for a tropical logging area. Top row: our *deadtrees.earth* Sentinel-2 fractional tree cover map for 13 June 2024 (left) and very-high-resolution optical imagery from Google Earth/Airbus (4 Nov 2023; contrast-stretched, right). Middle row: the first year in which the mapped fractional tree cover drops below 50% (left) and Global Forest Watch tree-cover loss year (right; (M. C. Hansen et al. 2013)). Bottom row: Tropical Moist Forests (TMF) first new disruption year within 2019 to 2024 (left; (Bourgoin et al. 2024; Vancutsem et al. 2021)) and RADD alert year (low & high confidence, right; (Reiche et al. 2021)), where green shading marks the forest baseline within which RADD issues alerts. All products share a common colour scale for 2019 to 2024; for Global Forest Watch and TMF, areas recorded as lost or disrupted before 2019 are shown in grey. All panels show the same spatial extent and projection (UTM zone 21N).

4.2 Case study 2: recovery and silviculture dynamics from time series (northern Germany)

Here we show how the annual time series resolves a full disturbance-to-recovery trajectory following a compound disturbance of fire, drought, and forest management, such as thinning. This site in northeastern Germany was initially dominated by Scots pine and was subject to several fires and silvicultural treatments (Heinken et al. 2024; Jouy et al. 2025; Schmehl et al. 2025). Ground-validated data was made available in Schmehl et al. 2025 and is displayed atop our generated multi-year maps in Figure 9.

The first fire occurred in August of 2018, shortly after the prediction date (center of leaf-on period) of the product in 2018. Accordingly, the extent of the fire is visible in the 2019 product in the form of both tree cover loss (compared to 2018) and a dense standing deadwood patch. The majority of the north-eastern forest was cleared before June 2019 (Heinken et al. 2024). In the southwestern part thinning and clear-cut was applied to selected plots (Schmehl et al. 2025) during autumn 2019, as it is evident by reduced fractional tree cover in 2020. In the most southern part of the 2019 burn extent, the fire was predominantly on the ground resulting in no immediate visible overstory mortality (dashed line in Figure 9, surface fire). Exceptional drought and infestation contributed to the die-off of those trees, as is visible in the standing deadwood product in 2020. A second fire lasted two days from June 17th to 19th in 2022, just after inference date, further decreased tree cover within the burn extent for 2023. The forest product shows an increase in the northern cover for the years 2024 to 2025 suggesting forest recovery was also visible in drone orthophotos in the same years. Overall, this case study demonstrates that combined mapping of tree and standing deadwood cover reveals fine-scale degradation patterns as well as recovery trajectories. In comparison, the European Forest Disturbance Atlas (Viana-Soto and Senf 2025) and Global Forest Watch (M. C. Hansen et al. 2013) only reveal that the location was disturbed but do not reflect mortality, thinning, or recovery dynamics (see Supplementary Figure S5a and Supplementary Figure S5b).

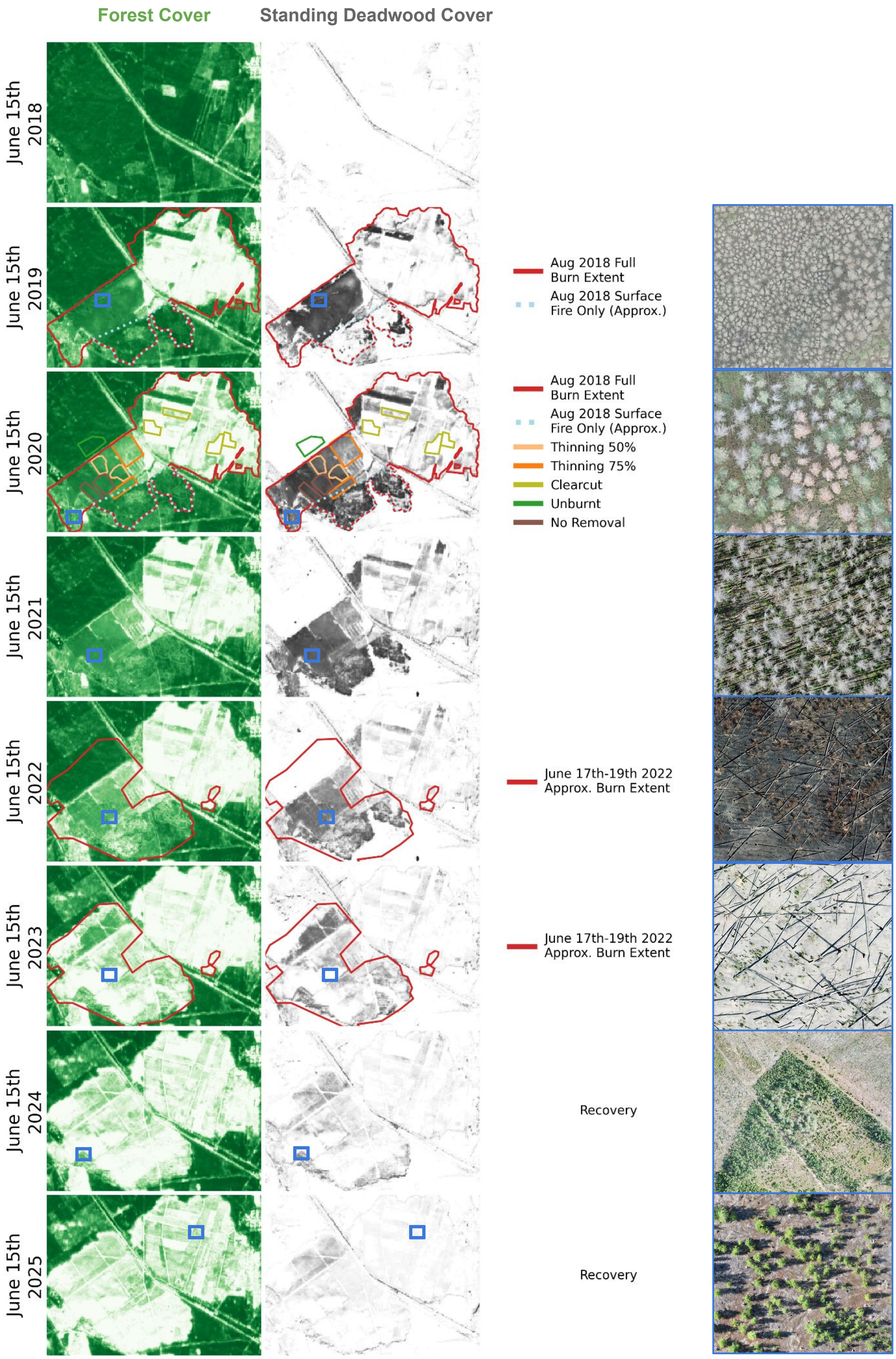

Figure 9: Fractional tree cover and standing deadwood product from 2018 to 2025 for a disturbance site in north-eastern Germany (52.04331°N, 12.92220°E). Ground-validated burn extent and monitoring plots on different silvicultural treatments were derived from Schmehl et al. 2025 (colored boxes in 2020). Rightmost column displays drone orthophotos within the respective year on multiple sites (blue).

4.3 Case study 3: mapping the timing of mortality (Saxon and Bohemian Switzerland, Germany and Czech Republic)

Standing deadwood persists for several years after tree death, so the annual time series can be reduced to the year in which mortality first became apparent. For Saxon Switzerland National Park and the adjoining Bohemian Switzerland National Park, we mapped for each pixel the first year in which standing deadwood cover exceeded 50% (Figure 10). The resulting map dates the bark beetle (*Ips typographus*) outbreak that killed much of the Norway spruce across both parks (Beetz et al. 2025; Pietzsch et al. 2023). Mortality became detectable in 2018, peaked in 2020 with 2515 ha, and declined steeply after 2022, consistent with progressive depletion of susceptible host trees. Newly affected area shifted from west to east over the course of the outbreak, resolving the direction in which the infestation advanced. At the stand level, mortality is resolved down to groups of a few pixels embedded in surviving canopy, and neighbouring patches frequently differ in the year they died (insets in Figure 10).

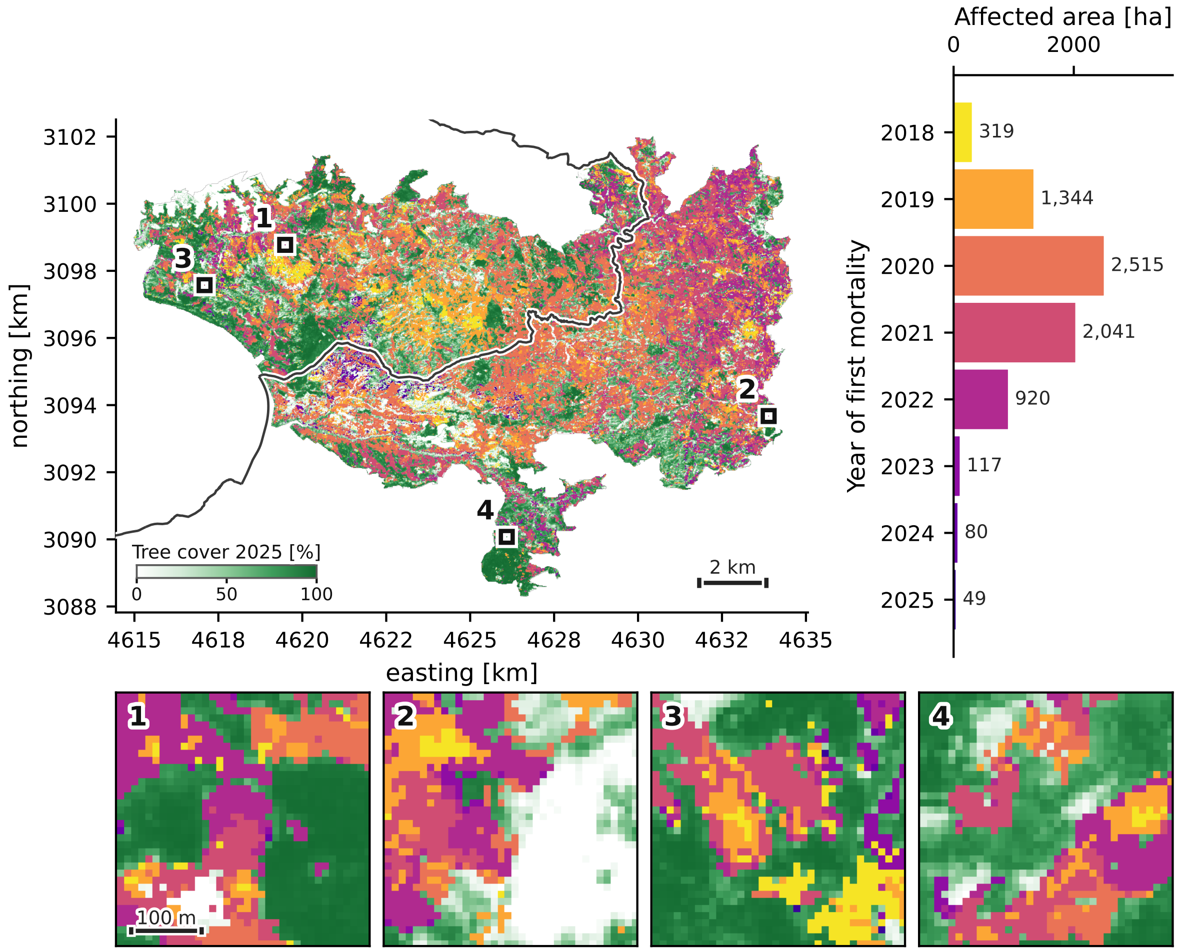

Figure 10: Timing of tree mortality across Saxon Switzerland National Park (Germany) and the adjacent Bohemian Switzerland National Park (Czech Republic), derived from the annual standing deadwood cover time series (10 m, EPSG:3035). Left: for each pixel, the first year in which mapped standing deadwood cover exceeded 50%, where the earliest class also contains pixels that crossed the threshold before 2018; pixels without such an event are shaded by their mapped tree cover for 2025. Right: forest area affected per year of first mortality, in colours shared with the map. Bottom: fine-scale detail at the four locations outlined on the map, all covering the same extent (scale bar in panel 1).

5 Discussion

In the following, we contextualize the scope, strengths, and limitations of the presented methodology. We first delineate the functional capabilities and inherent constraints of the methodology, discuss assumptions on phenological dynamics, forest structure, and georeferencing uncertainty. We then reflect on the length of satellite time series, evaluation limits imposed by weak supervision, and biome-specific performance patterns. Finally, we highlight research and operational applications enabled by globally consistent, annually resolved canopy-fraction products.

5.1 Scope of the resulting maps and methodological limitations

From a methodological perspective, the resulting annual maps are designed to represent canopy-level forest state and its evolution through time by jointly estimating fractional standing deadwood cover and fractional tree cover at 10 m resolution. This paired representation enables detection of top-of-canopy mortality signals (increases in standing deadwood cover) and subsequent tree loss (a decrease in tree cover), and, critically, allows these processes to be tracked as multi-year continuous trajectories rather than discrete classification of single-events. Because both variables are estimated as continuous sub-pixel fractions, the methodology can represent gradual disturbances and dieback within a pixel, as well as the subsequent recovery of tree cover during regrowth as crowns expand and gaps fill in. In addition, fractional tree cover provides an explicit measure of canopy openness, enabling differentiation between naturally open-canopy systems and dense, closed-canopy forests, which is important for interpreting disturbance impacts across biomes. Thus, the presented method provides sub-pixel metrics that enable year-over-year tracking of mortality, disturbance and recovery dynamics.

In this study, we assume that leaf-loss and browning in the leaf-on season is a reliable indicator of tree death (see Section 2). However, defoliation does not always indicate recent or proximate tree mortality. In some cases, trees may defoliate and refoliate within the same season, as observed in the response of *Pinus radiata* to the disease red needle cast (Dick et al. 2014; Watt et al. 2024), and of Mediterranean beach to a late frost (D'Andrea et al. 2019). In other cases, pest and pathogen impacts may be confined to the upper crown, such that residual or resprouting foliage persists below the dead crown and may be partially obscured in top-down imagery, causing stressed but living trees to appear dead when viewed from above. Although single defoliation events are often not sufficient to cause tree death, they can weaken trees, deplete carbohydrate reserves, and reduce growth rates, thereby increasing susceptibility to secondary stressors such as pests and diseases, and elevating tree mortality rates (Silvestro et al. 2025). While these phenomena complicate the detection of tree mortality, the temporal context of fractional yearly standing deadwood cover for relatively small areas aids in distinguishing temporary leaf-loss from continued leaflessness and death. Downstream analysis will need to take such phenomenon into account for accurate interpretation.

The proposed methodology maps and validates standing deadwood cover at the midpoint of the regional leaf-on season in each year. Leaf-on season is defined at the level of 40-km pixels, and thus encompasses regional and stand-level averages. However, leaf phenology including the timing of the leaf-on phase in deciduous individuals can vary substantially among species and trees within stands and regions, particularly in water-limited biomes (Park et al. 2026). This may partially explain the lower model performance in tropical or dryland ecosystems with high phenological variation within stands and/or among years (see Table 1). In these ecosystems, it is rarely immediately clear whether leaflessness corresponds to tree death, even with in-situ visual inspection. Furthermore, the regional mid-point leaf-on date may not be a useful point of reference for some trees and years, given complex and variable phenological patterns. Time series of standing deadwood cover and tree cover should nonetheless provide a solid basis for mapping tree mortality. We expect that mortality predictions will be improved in the future through development of more complex models incorporating finer temporal resolution and/or more detailed or adaptive phenological characterization.

Top-down optical imagery from drones and satellites has inherent limitations in detecting tree mortality in dynamic and multi-layered forest canopies. Aerial optical imagery is dominated by the top-most vegetation layer, and tree mortality in understory layers can be completely missed if the upper layer is unaffected. Even mortality in the canopy is harder to detect in multi-layered canopies, as disturbed patches can retain a green-dominated spectral signature if one or more understory layers remain (Coppin and Bauer 1996; Stephen Frolking et al. 2009). Further, rapid vegetation regrowth and ingrowth, often accompanied by rapid decomposition or collapse of canopy deadwood, can quickly erase any signal of canopy mortality events. Hence, substantial tree mortality may be accompanied by only small and transient shifts in cover (both standing deadwood and tree cover), which can be difficult to distinguish from seasonal deciduousness or other transient defoliation. As a result, it can be assumed that the method is only sensitive to fractional tree cover when the canopy gap fraction substantially increases (see Section 4.1 and Section 3).

5.2 The value of long spectral time series

Sentinel-2 lacks the spatial resolution that is necessary to explicitly resolve exact standing deadwood or tree cover within a given pixel, but it has the advantage of high temporal resolution which provides temporal context. This temporal information adds value in two distinct ways. First, the temporal trajectories in multispectral reflectance display the spectral fingerprint of forest dynamics. For example, a disturbance event in a temperate forest is expected to reveal itself as a sudden breakpoint in what would otherwise be a stable seasonal pattern (M. C. Hansen et al. 2013; Schiefer et al. 2023). Second,

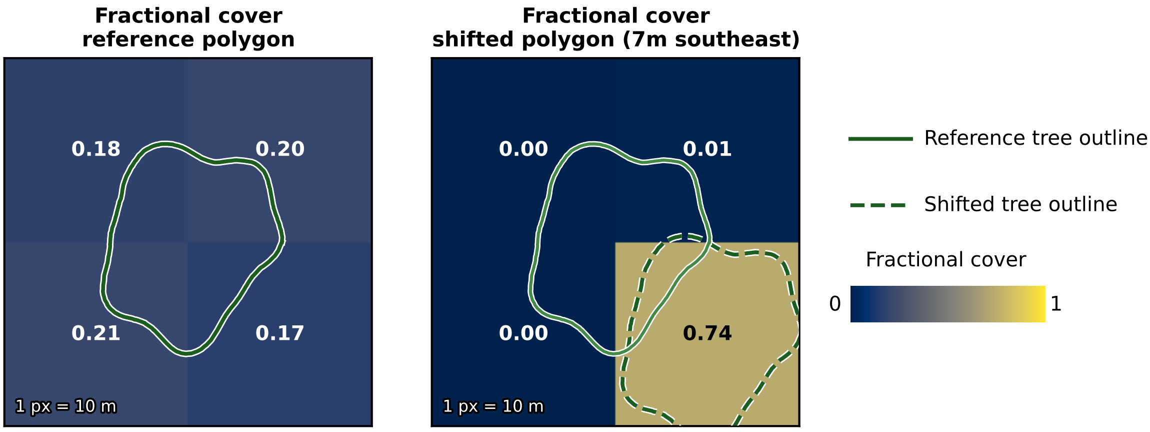

Figure 11: Illustration of how small spatial offsets propagate into large pixel-wise errors for 10 m fractional cover mapping. A single tree crown (solid outline) is converted to fractional cover in a 2 × 2 pixel window (left). Shifting the crown by 7 m southeast (dashed outline; right) changes the distribution of fractional cover across pixels, yielding an RMSE of 0.33 when comparing to the reference raster.

dense time series provide redundancy against reflectance variation unrelated to vegetation change, such as sensor noise, atmospheric scattering, or cirrus clouds, enabling more robust quantification of the target variable (Rußwurm and Körner 2020; Tseng et al. 2023). Together, these advantages help detect subtle changes and offset the coarse spatial resolution.

Our temporal context experiment showed the benefit of increased temporal resolution and extent (see Section 3.3). In the context of deep learning and vegetation mapping from Sentinel-2 time series, mostly time spans of up to two years are considered (Montero et al. 2024a, 2025; Rußwurm and Körner 2020; Schiefer et al. 2023; Tseng et al. 2023; H. K. Zhang et al. 2025). Our findings highlight that the first year of historical temporal context is the most critical, but additional years further boost the performance for standing deadwood cover estimation. We hypothesize that for standing deadwood longer timeseries are more important as they can capture the sudden or gradual death process. All experiments used four weeks to four years of context before the disturbance, so they quantify the value of pre-disturbance temporal context but not single-timestep baselines or post-disturbance observations.

5.3 Evaluation limits from georeferencing uncertainty

Because the georeferencing of both Sentinel-2 observations and crowd-sourced drone orthophotos is only accurate to the meter scale, the training and evaluation targets are both approximate, making model training a weakly supervised task. To bound this uncertainty, *deadtrees.earth* retains only orthophotos with less than 15 m offset relative to publicly available aerial basemaps (Mosig et al. 2026). For Sentinel-2, Copernicus reports < 12 m absolute geolocation error at 95.5% confidence, < 5 m multitemporal registration error at 95.5% confidence, and < 0.3 px multispectral registration error at 99.7% confidence (Choi et al. 2025; Copernicus n.d.). Even within these bounds, small spatial shifts can strongly affect pixel-wise fractional cover labels: a shift of only 7 m can redistribute cover across adjacent 10 m pixels and substantially change per-pixel values, which is particularly consequential for scattered standing deadwood and very sparse forests (Fig. 11). As a result, pixel-to-pixel evaluation can overestimate error and imposes an upper bound on model performance scores even with infinite model capacity and training data. Across the full dataset, for a pixel-to-pixel evaluation we obtained weighted RMSE values of 0.41 for standing deadwood cover and 0.25 for tree cover (mean across biomes) Table 1.

In contrast, spatial shifts conserve area totals, such that large-area bias estimates are considerably more stable: at biome level, our model overestimated standing deadwood cover by only 4% and underestimated tree cover by 6% Table 1, where tree cover underestimation is driven by little sensitivity to crown gaps of the drone tree segmentation model (see Section 2.1.1). This indicates that further improvements in pixel-level correlation or mean-error metrics are not necessarily the most meaningful optimization target. Consistently, aggregating predictions to coarser 50 and 100 m grids reduces the effect of these sub-pixel offsets and improves the agreement between predictions and reference (Section A.7). The issue is exacerbated for binary disturbance products (disturbed/intact), where a meter-scale shift near the presence/absence threshold flips the entire class label rather than changing a value incrementally (Alix-Garcia and Millimet 2023), an all-or-nothing error that is most consequential for sparse or scattered targets; such maps remain common in operational monitoring (M. C. Hansen et al. 2013; Viana-Soto and Senf 2025). Future work should consider training and evaluation protocols that account for georeferencing uncertainty rather than enforcing strict per-pixel agreement (Mnih and Hinton 2012); our preliminary adaptation to sub-pixel shifts produced smoother maps without improving accuracy (not shown). Lastly, these georeferencing uncertainties are partly mitigated by scale: as the reference archive expands across regions and years, the model can learn invariant temporal–spectral patterns and become increasingly robust to geolocation offsets.

The performance metrics we report characterize model error on the reference dataset, not the accuracy of a wall-to-wall map. Because the *deadtrees.earth* orthophotos are contributed opportunistically rather than drawn as a spatially representative probability sample, the cross-validation scores reflect how well the model reproduces sub-pixel cover where reference data happen to exist, and need not carry over to regions or conditions that the archive underrepresents (Meyer and Pebesma 2022). Although we make wall-to-wall maps available through *deadtrees.earth* for comment by the research community, these must be interpreted with caution.

5.4 Current model capabilities, limitations, and future model improvements

Precisely mapping fractional cover from Sentinel-2 in scattered-mortality or open-canopy settings is challenging because tree crowns are often smaller than the 10 m pixel (Jucker et al. 2025), and a pixel's reflectance mixes signals from neighboring pixels (Choi et al. 2025) and varies with georeferencing shifts and site conditions (stand structure, understory, heterogeneity) unrelated to the cover value (also see Section 5.3). Despite these challenges, we observed consistent precision and recall performance for cover values above 50%, where the model generally performed much better for tree cover than standing deadwood (see Figure 4).

Performance however rapidly decreased for low fractional cover values ($< 50\%$, also see Figure 1), especially for standing deadwood. A key difference between tree and standing deadwood cover was reference data availability. Overall, the available training data for fractional tree cover was about 5 times larger than for standing deadwood cover (7.27 vs. 1.37 million pixels for cover $> 0\%$) and about 91 times larger for cover values above 50% (4.55 vs. 0.05 million for cover $> 50\%$). This inequality is naturally inherited from the problem definition where standing deadwood cover is a subset of tree cover, and most sites only have low levels of tree mortality.

The model performed worse in tropical and boreal forests than in other biomes. In these forests, reliably mapping standing deadwood, especially scattered deadwood, remained challenging due to limited cloud-free observations (see Supplementary Figure S6). In the tropics specifically, this is likely exacerbated by strong vertical vegetation stratification, high phenological heterogeneity, and predominantly scattered mortality patterns (Espírito-Santo et al. 2014; Xu et al. 2026). For boreal forests, smaller crowns and generally more open canopy forests with lower tree cover likely increase the difficulty. Lastly, reference data on standing deadwood was comparably underrepresented in both biomes, showing promising room for future improvement. As our spatial block cross-validation (Ploton et al. 2020; Roberts et al. 2017) evaluates on spatially independent held-out regions, we attribute this gap to sparse training data preventing the model from learning the specific features of these biomes.

In both the reference data and the model predictions, standing deadwood cover above 70% was rare in non-temperate biomes, so precision and recall could not be estimated reliably at such high cover there (see Figure 4 and Section 2.2.6). This scarcity is only partly a dataset gap (Supplementary Figure S7); to a large extent it reflects a genuine ecological ceiling on how high fractional deadwood cover can become in these biomes. Because standing deadwood cover cannot exceed tree cover, open-canopy systems such as drylands and boreal woodlands, where tree cover is well below 100%, cap the attainable deadwood fraction: even complete die-off of a woodland with 50% tree cover yields at most about 50% deadwood cover. In addition, where mortality is scattered rather than stand-replacing, individual dead crowns rarely fill an entire 10 m pixel, so high per-pixel fractions occur only occasionally, when crown and pixel boundaries happen to align (see Figure 11).

Taken together, these patterns suggest that the main limitations can be attributed to underrepresented regions and conditions, and should resolve with a more comprehensive training data set. Each new contribution to the database platform *deadtrees.earth* has the potential to improve the robustness and generalization capabilities of the model. Commonly, training datasets are created and harmonized only once as a preprocessing step. However, in this work, the data flow and balancing scheme during model training was specifically designed to dynamically scale with the growing archive of drone data (see Section 2.2.5). Both tree cover and standing deadwood segmentation models can be automatically applied to new data. Sentinel-2 data preprocessing is automated through *sentle* (github.com/cmosig/sentle). In total, apart from manual quality checks of new contributions and automated segmentations, the presented overall workflow enables regular and automatic model retraining, such that every new drone orthophoto can improve the Sentinel-2 based maps.

Compared to existing state-of-the-art continental-scale products, our model showed qualitatively better agreement with the reference data in the case studies (see Section 4.1 and Section A.3), capturing gradual change and partial disturbances that binary disturbance masks miss and distinguishing canopy-visible mortality from subsequent tree loss. For fractional tree cover, a quantitative comparison against the Global 30 m Landsat Tree Canopy Cover (Sexton et al. 2013) and Copernicus Tree Cover Density (Copernicus Land Monitoring Service 2020) products, evaluated on identical held-out cells, shows closer agreement of our estimates with the drone reference (Section A.6). The disturbance-product comparisons remain qualitative and limited to a small set of sites; future work should therefore focus on exhaustive quantitative benchmarking against disturbance products and centimeter-scale, ground-validated data across disturbance types, severities, and biomes.

5.5 Applications of map products beyond quantification

Applied across the full Sentinel-2 archive, the single-year cover estimates form annual time series of tree and standing deadwood cover, from which a range of disturbance and mortality dynamics can be derived (Section 4). Because the maps separate standing mortality from tree loss, disturbances can be attributed to causes such as fire, harvest, or drought, and recovery rates and standing-deadwood persistence can be quantified. Such trajectories also inform carbon-cycle assessments, where mortality can flip ecosystems from carbon sinks to sources (Migliavacca et al. 2025b; Schulze 2006; Wijas et al. 2024), while current-year mortality maps can act as early-warning signals for insect outbreaks in remote regions and guide ground or aerial surveys (Korznikov et al. 2025; U.S. Forest Service 2025). Beyond disturbance, the globally consistent tree cover maps can inform research on treelines, forest fragmentation, and trees outside forests (Garbarino et al. 2023; Liu et al. 2023), and, requiring no external forest mask, serve as priors or training targets for weakly supervised segmentation in higher-resolution imagery (Schmitt et al. 2020).

6 Conclusion

We introduce a methodology to map yearly fractional tree cover and fractional standing deadwood cover at 10 m resolution (2018–2025) from four-year Sentinel-2 multispectral pixel time series. We trained and evaluated the satellite-based models with centimeter-scale drone orthophotos from *dead-trees.earth*, which were used to create a globally distributed standing deadwood cover and tree cover dataset using semantic segmentation models. This represents the first globally consistent mapping approach that simultaneously tracks fractional tree cover and standing deadwood cover across biomes, thereby enabling new perspectives on disturbance trajectories and post-disturbance ecosystem dynamics.

Across biomes, the satellite-based models reproduced tree cover more accurately than standing deadwood cover, with clear biome dependence and the expected sensitivity to reference data availability. We show that the length of satellite time series has a strong imprint on the model performance, highlighting the value of continuous Earth observation products. Multiple case studies indicate that the maps recover known, fine disturbance patterns and timing with higher sensitivity to fine-scale dynamics compared to existing state-of-the-art disturbance products. Together with the open processing stack, this methodology provides a path towards globally consistent fine-scale disturbance metrics for ecology, carbon cycle studies, risk assessment, and targeted field campaigns.

Code and Data Availability

The Sentinel-1 and -2 processing pipeline (see Section 2.1.3) is publicly available in the form of a python package: github.com/cmosig/sentle. The version used in this paper is 2025.10.1. The code to reproduce the results and the model will be made public after acceptance of the manuscript. The preprocessed training dataset including Sentinel-2 data and references rasters will be made available after the acceptance of the manuscript. Previews of tree cover and standing deadwood cover maps generated with the introduced methodology will be made available and continuously updated on deadtrees.earth/deadtrees.

Declaration of generative AI and AI-assisted technologies in the manuscript preparation process.

During the preparation of this work the author(s) used ChatGPT for language editing. During analysis, the authors employed GitHub Copilot and OpenAI Codex for programming assistance. After using these tools, the author(s) reviewed and edited the content and code as needed and take(s) full responsibility for the content of the published article and code.

Acknowledgements

C.M., T.K., M.D.M., J.V.J. thank the European Space Agency for funding the "DeepFeatures" project via the AI4SCIENCE activity and the "FORTRACK" project via the ESA CLIMATE SPACE: Climate-Biodiversity studies. C.M. and M.D.M. acknowledge financial support from the German Aerospace Centre (DLR) on behalf of the Federal Ministry for Economic Affairs and Climate Action (BMWK) for project ML4Earth (FKZ 50EE2201B). T.K. and J.S. acknowledge funding from the German Research Foundation via the "PANOPS" (grant no. 504978936) and EXC 3127 Future Forests. T.K., J.V.J. and S.S. acknolwedge support by the Ministry for Food, Rural Areas, and Consumer Protection, Baden-Württemberg, Germany (grant no. 52-8670.00) and the German Research Foundation via the NFDI4Earth pilot project GeoLabel (DFG grant no. 460036893). K.K. acknowledges the financial support from the Czech Science Foundation (25-15727S). D.N. was partially supported by the European Union's Horizon Europe Research and Innovation Programme under grant agreement 101134200 "Forest surveillance with artificial intelligence and digital technologies – FORSAID". MB acknowledges support from SNSF-Sinergia grant number CRSII5_216562 and SNSF grant number IZCOZ0_213355. S.H. and Y.C. acknowledged funding from Villum Fonden (DRYTIP project, grant agreement no. 37465). We thank Clement Bourgoin for his help in the correct interpretation of the Tropical Moist Forests (TMF). We thank Ian McGregor and Evan Gora of the Cary Institute of Ecosystem Studies for providing helpful insights and perspectives about mortality and tree loss detectability with this approach on Barro Colorado Island.

A Appendix

A.1 Center of leaf-on period global map

Supplementary Figure S1 maps, for each location, the phenology-derived day-of-year on which the Sentinel-2 time series is centered (see Section 2.1.2).

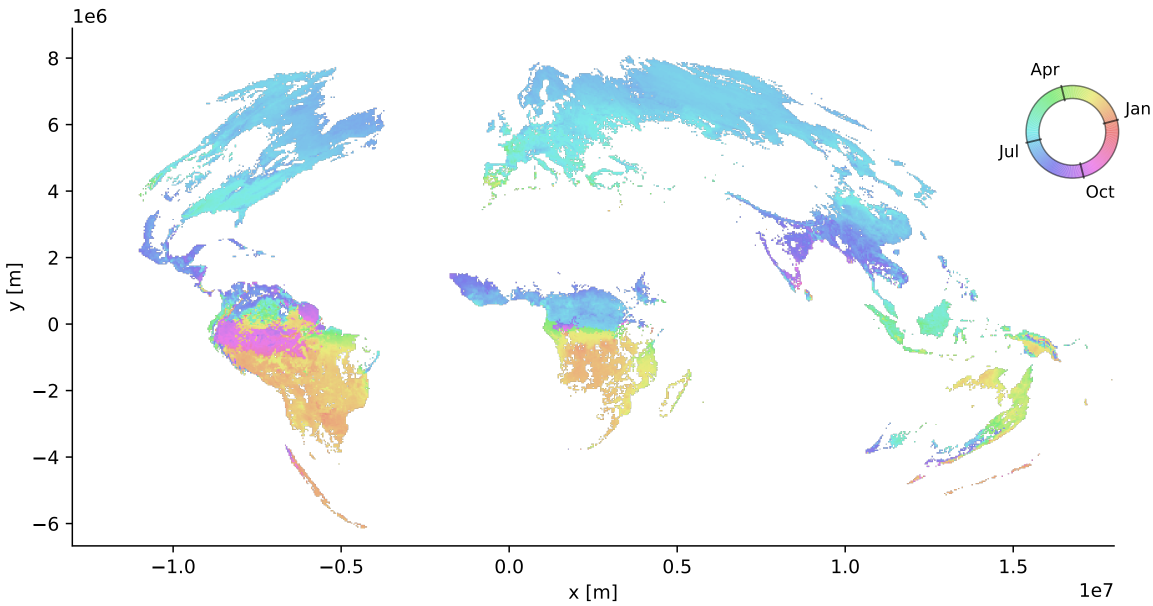

Figure S1: Computed training and inference day-of-year (see Section 2.1.2) based on phenology indicator on *deadtrees.earth* (Mosig et al. 2026). Projection is MODIS Sinusoidal (ESRI:54008).

A.2 Case study: insect-driven mortality in boreal taiga (Sakhalin, Russia)

This collection of tree mortality sites is located on Sakhalin Island (Russia), in the Northwest Pacific region, a boreal taiga biome (Korznikov et al. 2022, 2025). The sites were first delineated through Pléiades-2, WorldView-2, and WorldView-3; and subsequently confirmed on the ground by local researchers. Further, the local surveys identified the affected tree species and the mortality agent (see Supplementary Table S1).

The model mapped a standing deadwood cover above $\geq 20\%$ for 74%, 92%, 99%, and 1% of the affected area across the sites A-D, respectively. The site that was affected by silkworms (site D) obtained fractional cover values averaging 1.4% standing deadwood and 30% for tree cover, thus not mapping the standing deadwood correctly. It is worth noting that the silkworm infestation happened before the Sentinel-2 launch between 2011 and 2014, and hence within the temporal spectral context,

Table S1: List of ground validated sites on Sakhalin Island (Russia). Column year denotes year of observation and map creation. Observation (Obs.) is the date where the observation was confirmed on the ground. Inference (Inf.) date is the date where the product was created on the respective location. Bark beetle refers to *Ips typographus*, silkworm refers to *Dendrolimus superans*. Species names: spruce – *Picea jezoensis*, *Picea glehnii* (only in the cite C), fir – *Abies sachalinensis*, larch – *Larix gmelinii*

.

Site	Year	Obs. date	Inf. date	Affected species	Mortality agent	Centroid
A	2020	Sep 12th	Jul 5th	Spruce	bark beetles	142.6205°N 47.4857°E
B	2021	Jun 9th	Jul 5th	Spruce	bark beetles	142.4572°N 47.4134°E
C	2021	Aug 2nd	Jul 1st	Spruce	bark beetles	141.9992°N 47.4586°E
D	2018	Jul 9th	Jul 15th	Fir, Spruce, Larch	silkworms	142.0757°N 48.5547°E

the trees were not alive at any point and only standing deadwood. All sites affected by bark beetles were accurately recovered by the model and mapped outbreak patches closely matched the provided polygons (see Supplementary Figure S2). In comparison, Global Forest Watch (M. C. Hansen et al. 2013) recorded loss at all four sites over its full 2001–2024 record, but covering only part of the delineated mortality, and it dates the loss at site D to 2011–2013 (rightmost column of Supplementary Figure S2), consistent with the silkworm infestation preceding the Sentinel-2 archive. Note that the provided data only report tree mortality within the delineated sites; it cannot be assumed that tree mortality is absent in regions outside the polygons.

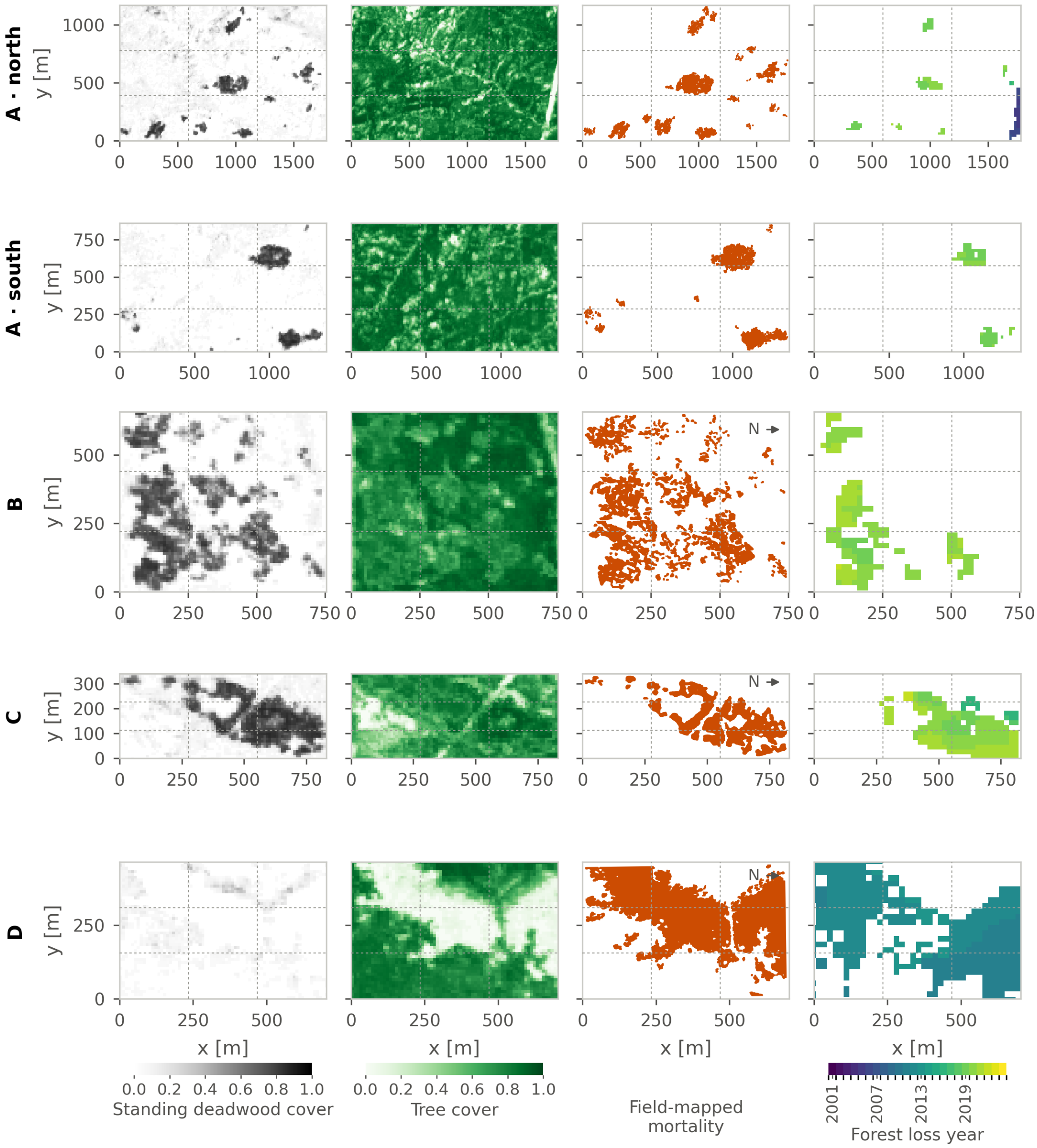

Figure S2: Ground-validated tree mortality sites A–D on Sakhalin Island (Russia; see Supplementary Table S1). Rows show the four sites, with site A split into its northern and southern cluster. Columns show, from left to right, the mapped fractional standing deadwood cover (grey scale) and the mapped fractional tree cover (green scale), both for the inference year of the respective site; the mortality delineated in the field by local experts; and the year of forest loss recorded by Global Forest Watch (M. C. Hansen et al. 2013) over its full 2001–2024 record. The third column is the reference against which the mapped covers are compared and shows the delineation at its full resolution; the remaining columns carry no overlay, so the mapped values remain fully visible. Dashed guides mark identical positions in every panel of a row to aid comparison across columns. All panels of a row share the same extent, and axes are metres relative to the lower-left corner of that window.

A.3 Case study supplements: field inventory, plot locations, and comparison with existing products

Following a bark beetle outbreak, three areas in the Italian Alps were surveyed with drones (about 100 ha per area were covered) in June 2024. A ground survey of 20 plots in total was performed within the surveyed area in October 2024. In each plot, approximately 1 ha in size, the surveyors labeled each tree in the June drone imagery by recording the state of mortality and tree species. The dominant tree species on these plots were *Picea abies* (64%), *Abies alba* (20%), *Fagus sylvatica* (11%), and *Larix decidua* (2%). For the same sites we mapped standing deadwood cover and tree cover for June 5th 2024 (maximum greenness day of year).

Comparisons of the field recorded state of mortality with Sentinel-2 mapped fractional cover yielded strong overlaps (see Supplementary Figure S3). The dense tree mortality hotspot was recovered in the maps. For the plots Asiago-1, Asiago-14, and Visdende-5, the model mapped tree mortality with low standing deadwood cover ($< 50\%$) where there were only healthy trees present in the survey. For the sites Visdende-2, Ciapela-1, and Ciapela-3 the mapped cover is consistently shifted by $5 - 10$ m, which is within expectation of the registration accuracy of Sentinel-2.

In comparison, the European Forest Disturbance Atlas (Viana-Soto and Senf 2025) and Global Forest Watch (M. C. Hansen et al. 2013) do show coarse disturbance signals for a subset of patches, while the majority of scattered mortality is not mapped (see Supplementary Figure S4a and Supplementary Figure S4b). Supplementary Table S2 lists the centroid coordinates of the plots surveyed in this field inventory.

Table S2: Centroid locations of each plot in the forest inventory comparison of Section A.3.

Plot Name	Number	Centroid	Plot Name	Number	Centroid
Asiago	1	45.9384°N 11.6252°E	Ciapela	2	46.4222°N 11.9261°E
Asiago	2	45.9377°N 11.6223°E	Ciapela	3	46.4235°N 11.9286°E
Asiago	3	45.9336°N 11.5993°E	Ciapela	4	46.4217°N 11.9310°E
Asiago	4	45.9375°N 11.6158°E	Ciapela	5	46.4233°N 11.9255°E
Asiago	5	45.9389°N 11.6145°E	Ciapela	6	46.4189°N 11.9361°E
Asiago	9	45.9362°N 11.6110°E	Visdende	1	46.6195°N 12.6587°E
Asiago	10	45.9367°N 11.6048°E	Visdende	2	46.6140°N 12.6528°E
Asiago	13	45.9333°N 11.6041°E	Visdende	3	46.6133°N 12.6559°E
Asiago	14	45.9342°N 11.6171°E	Visdende	5	46.6212°N 12.6590°E
Ciapela	1	46.4204°N 11.9337°E	Visdende	6	46.6180°N 12.6581°E

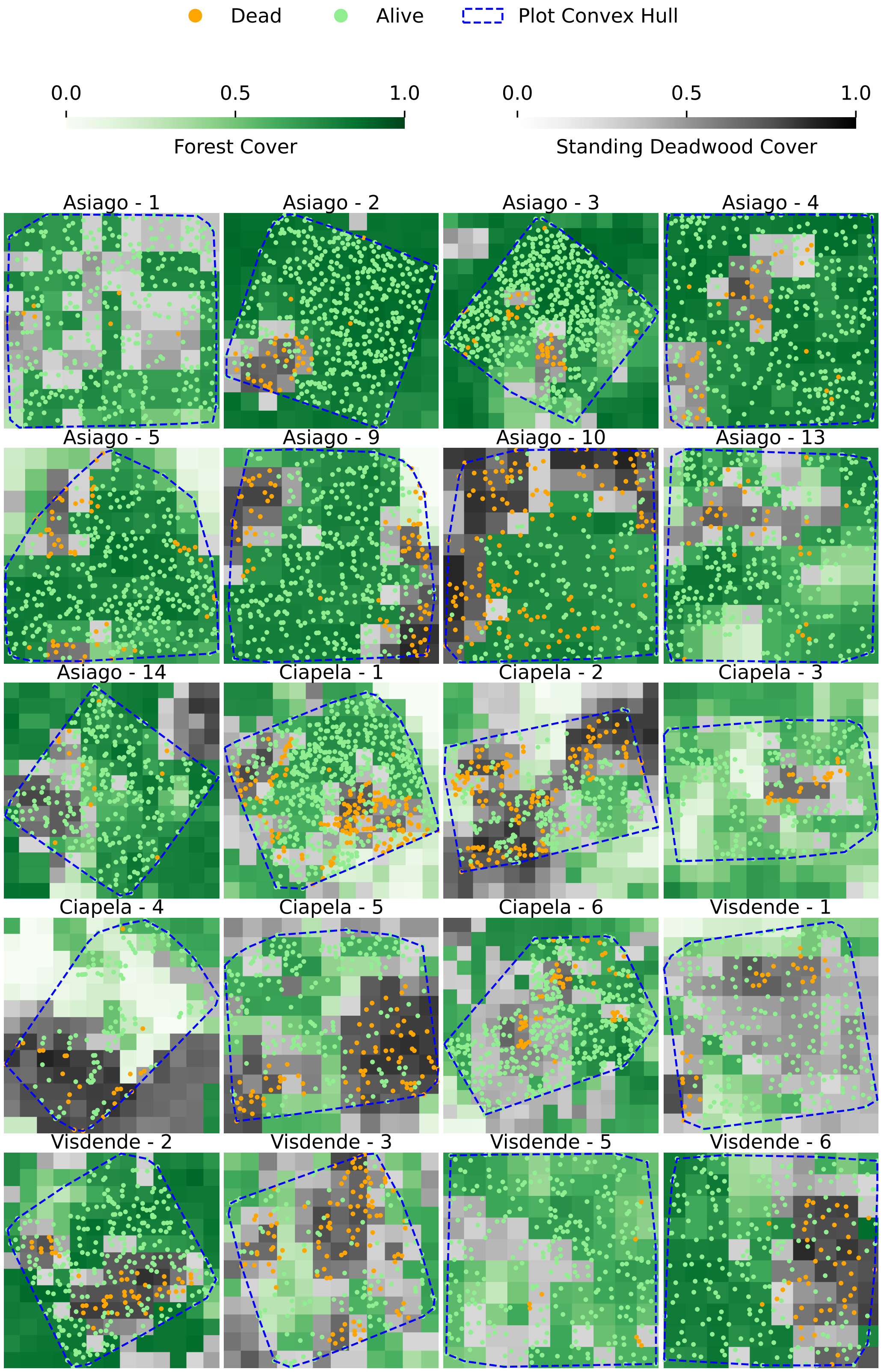

Figure S3: Comparison of mapped standing and tree cover against field-inventory for 20 plots in northern Italy in 2024. Each point corresponds to a tree, where dead trees are marked with orange and green otherwise. Mapped standing deadwood cover is displayed atop tree cover for pixels where the mapped deadwood cover was larger than 25%. The bounds of each plot are denoted by the convex hull (blue). Centroid locations in Supplementary Table S2.

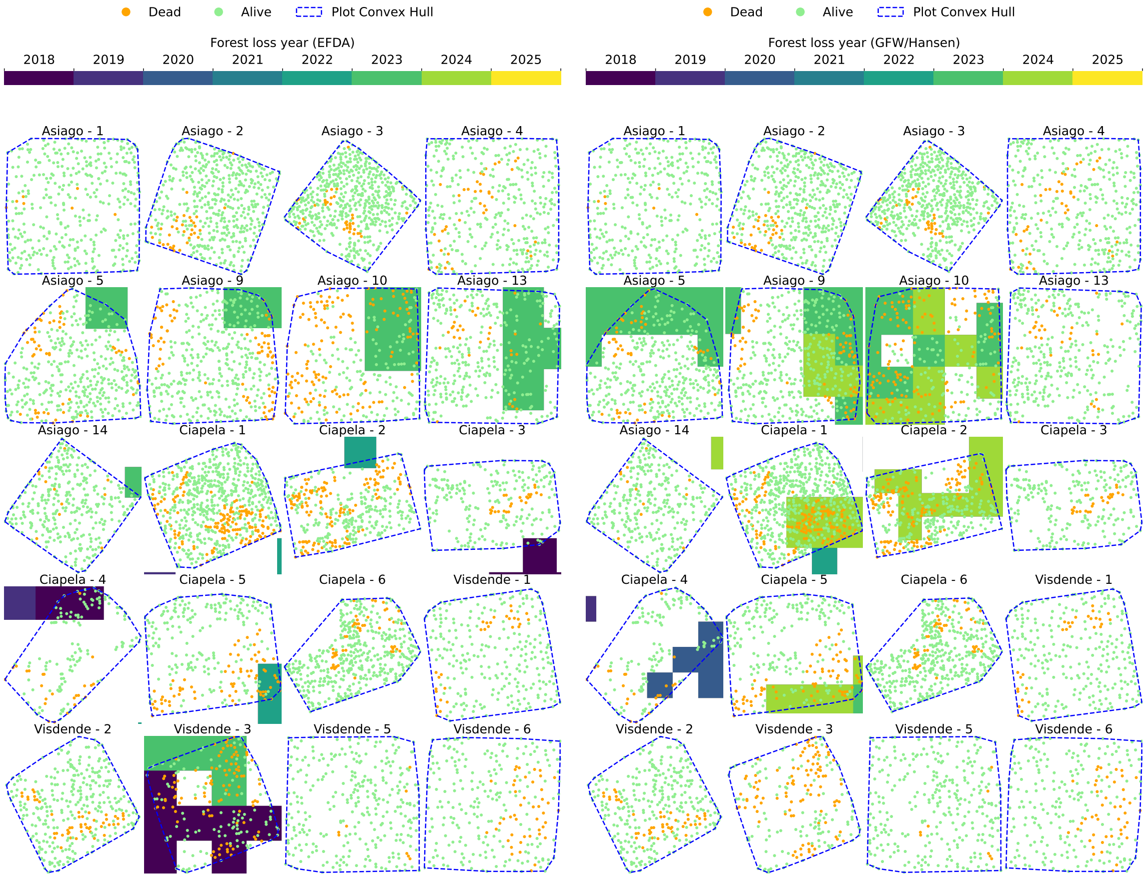

(a) EFDA (Viana-Soto and Senf 2025).

(b) GFW (M. C. Hansen et al. 2013).

Figure S4: Italian Alps forest inventory: Identical visualization to Supplementary Figure S3 but disturbance map was obtained from Global Forest Watch (GFW) (M. C. Hansen et al. 2013) and European Forest Disturbance Atlas (EFDA) (Viana-Soto and Senf 2025).

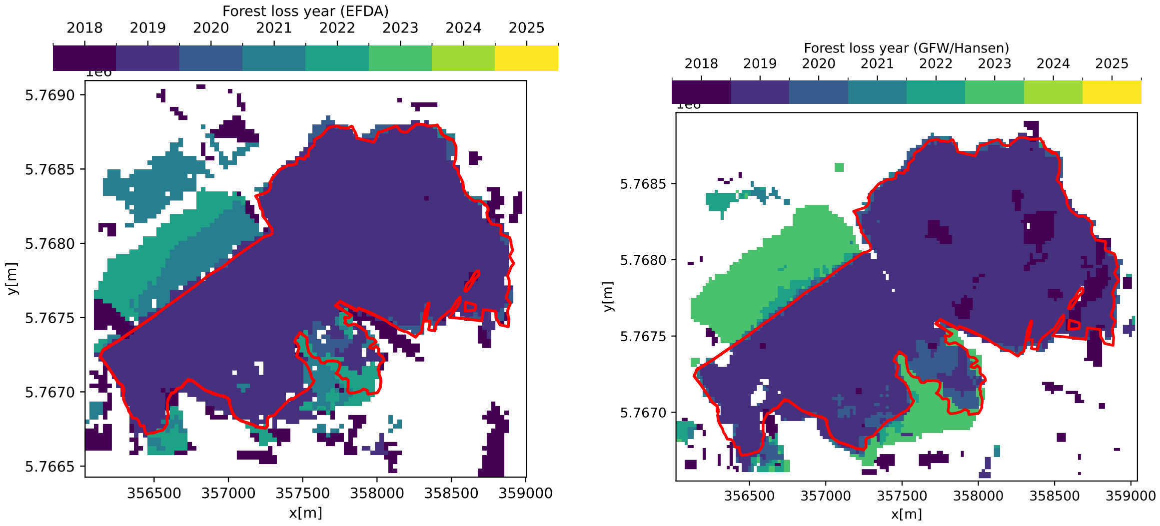

(a) EFDA (Viana-Soto and Senf 2025).

(b) GFW (M. C. Hansen et al. 2013).

Figure S5: Northern Germany case study: Aggregated visualization for site in Section 4.2, with disturbance map from obtained from Global Forest Watch (GFW) (M. C. Hansen et al. 2013) and European Forest Disturbance Atlas (EFDA) (Viana-Soto and Senf 2025). Red line shows extent of fire for 2018 (see Section 4.2).

A.4 Number of available timesteps per biome per year

Supplementary Figure S6 shows the distribution of cloud- and snow-free Sentinel-2 observations per year across biome groups.

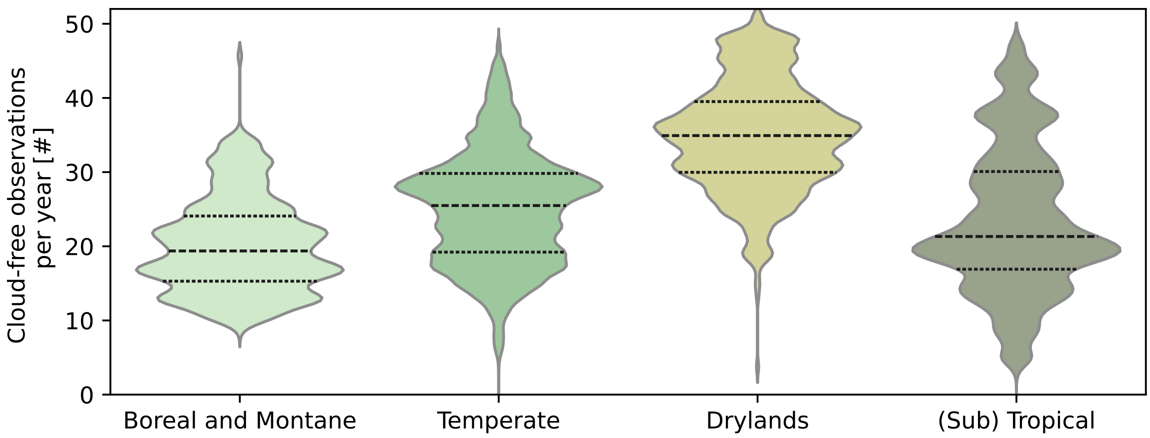

Figure S6: Violinplot of cloud-free and snow free observations per year across biome groups, where plot width depicts kernel density estimate. Dashed lines corresponds to median (thick dashed) and 25th and 75th quantile (thin dashed).

A.5 Reference label distribution per cover class

Complementing the spatial distribution of reference data (Figure 3), Supplementary Figure S7 shows how the reference labels are distributed across fractional cover values, separately for tree and standing deadwood cover and broken down by biome. Both classes are strongly imbalanced toward low cover, most pronounced for standing deadwood, which motivates the bin-resampling applied during evaluation (see Section 2.2.6).

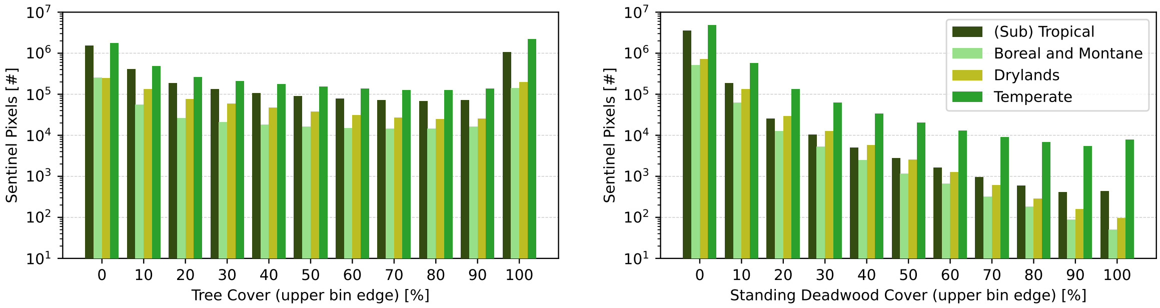

(a) Tree cover. (b) Standing deadwood cover.

Figure S7: Number of labeled Sentinel-2 pixels per 10% fractional cover bin (upper bin edge), broken down by biome, for (a) tree cover and (b) standing deadwood cover across the full dataset, i.e., the same reference data shown spatially in Figure 3. Note the logarithmic y-axis.

A.6 Comparison with existing fractional tree cover products

We benchmark our fractional tree cover against two existing products that report per-pixel tree cover as a fraction: the Global 30 m Landsat Tree Canopy Cover product (GFCC, epoch 2015) (Sexton et al. 2013) and the Copernicus Land Monitoring Service Tree Cover Density product (TCD, 10 m, Europe) (Copernicus Land Monitoring Service 2020). Both products and our model are evaluated against the same drone-derived tree cover labels on the held-out cross-validation test folds, over the identical set of cells where the respective product is valid. Our model and the drone labels are aggregated from their native 10 m grid to the product support (30 m for GFCC, native 10 m for TCD) by averaging the 10 m values within each cell. Each product is resampled onto our cell centres by reprojecting the cell centre and nearest-neighbour sampling the product (GFCC in EPSG:4326, TCD in EPSG:3035); the product percentages are rescaled to $[0, 1]$ and nodata cells are dropped. For GFCC we use the 2015 epoch, the closest available to the 2018–2024 drone acquisitions; for TCD we use the yearly layer closest to each site's acquisition year.

Against the drone labels, our model agrees better than either product (Supplementary Table S3,

Table S3: Tree-cover agreement at 30 m against drone labels for our model and GFCC30TC (2015), on the held-out cross-validation test set: mean (std) across folds of bin-resampled weighted Pearson's r, weighted RMSE, and mean error (ME). Both methods use the identical set of 30 m cells where GFCC is valid.

Biome	Metric	Our Model (30 m)	GFCC (30 m)
(Sub) Tropical	Pearson	0.71 (0.04)	0.40 (0.07)
	RMSE	0.22 (0.01)	0.39 (0.03)
	ME	-0.00 (0.03)	-0.16 (0.03)
Boreal and Montane	Pearson	0.72 (0.04)	0.37 (0.07)
	RMSE	0.21 (0.01)	0.34 (0.04)
	ME	-0.01 (0.05)	-0.13 (0.10)
Drylands	Pearson	0.75 (0.05)	0.43 (0.16)
	RMSE	0.21 (0.01)	0.41 (0.03)
	ME	-0.03 (0.03)	-0.18 (0.09)
Temperate	Pearson	0.74 (0.01)	0.39 (0.04)
	RMSE	0.21 (0.00)	0.33 (0.01)
	ME	-0.01 (0.02)	-0.13 (0.03)
All	Pearson	0.73 (0.02)	0.40 (0.03)
	RMSE	0.21 (0.01)	0.35 (0.01)
	ME	-0.01 (0.01)	-0.15 (0.02)

Supplementary Table S4, Supplementary Figure S8, and Supplementary Figure S9). At 30 m across all sites, our model reaches a weighted Pearson's r of 0.73 and RMSE of 0.21, compared to $r = 0.40$ and RMSE $= 0.35$ for GFCC, which also systematically underestimates tree cover (ME $= -0.15$). At 10 m over the European sites, our model reaches $r = 0.68$ and RMSE $= 0.23$, compared to $r = 0.38$ and RMSE $= 0.48$ for TCD. Two caveats apply. The Copernicus TCD comparison is restricted to the subset of European sites where the product is spatially and temporally available, and there our model and TCD are evaluated on exactly the same cells. The GFCC comparison instead uses all sites globally, with the caveat that its 2015 epoch can precede the 2018–2024 drone reference by up to about a decade, so part of the disagreement reflects real forest change rather than product error.

Table S4: Tree-cover agreement at 10 m against drone labels (European sites) for our model and Copernicus Tree Cover Density (yearly, matched to acquisition year), on the held-out cross-validation test set: mean (std) across folds of bin-resampled weighted Pearson's r, weighted RMSE, and mean error (ME). Both methods use the identical set of 10 m cells where TCD is valid.

Biome	Metric	Our Model (10 m)	Copernicus TCD (10 m)
Boreal and Montane	Pearson	0.64 (0.10)	0.49 (0.12)
	RMSE	0.24 (0.03)	0.40 (0.23)
	ME	-0.02 (0.05)	0.04 (0.15)
Drylands	Pearson	0.72 (0.05)	0.50 (0.12)
	RMSE	0.22 (0.02)	0.31 (0.05)
	ME	-0.04 (0.06)	-0.09 (0.06)
Temperate	Pearson	0.67 (0.02)	0.35 (0.18)
	RMSE	0.23 (0.01)	0.54 (0.23)
	ME	-0.05 (0.02)	0.02 (0.10)
All	Pearson	0.68 (0.02)	0.38 (0.15)
	RMSE	0.23 (0.01)	0.48 (0.19)
	ME	-0.05 (0.02)	0.01 (0.08)

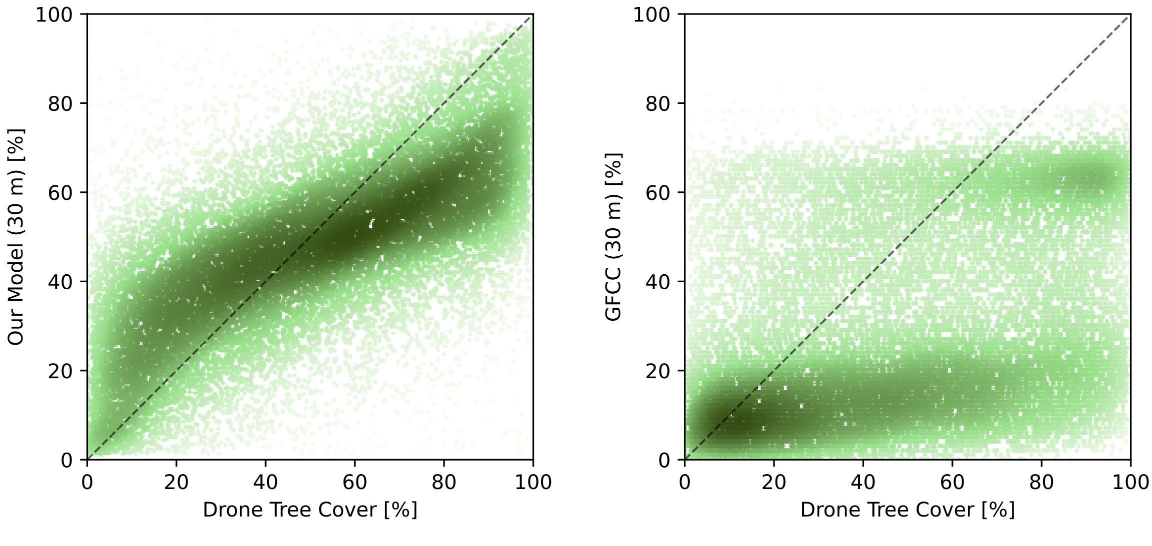

(a) Our model.

(b) GFCC (2015).

Figure S8: Predicted versus drone-derived tree cover at 30 m on the held-out test set, for (a) our model and (b) GFCC (Sexton et al. 2013), over the identical set of 30 m cells. Dashed line is the 1:1 relation; shading shows point density.

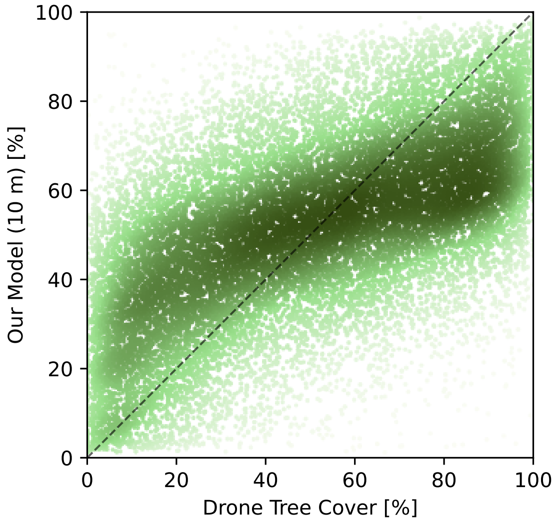

(a) Our model.

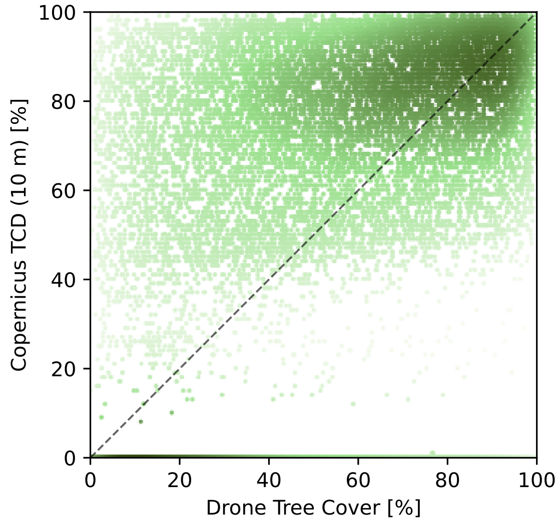

(b) Copernicus TCD.

Figure S9: Predicted versus drone-derived tree cover at 10 m on the held-out European test sites, for (a) our model and (b) Copernicus TCD (Copernicus Land Monitoring Service 2020), over the identical set of 10 m cells. Dashed line is the 1:1 relation; shading shows point density.

A.7 Predicted-versus-reference agreement and spatial aggregation

We assessed per-pixel agreement between predicted and drone-derived reference cover on the held-out cross-validation test folds, separately for tree and standing deadwood cover, with each pixel scored only by the fold in which it was never used for training. To visualise the joint distribution without the dominant low-cover pixels saturating the display, points are resampled to a uniform marginal along the reference axis (1%-wide reference bins, 200 points drawn per occupied bin) and coloured by local density (Gaussian kernel-density estimate, plotted in ascending density order); the dashed 1:1 line marks perfect agreement. The orange line with circular markers is the binned conditional mean of the prediction: for each 5%-wide reference-cover bin, the mean prediction computed on the raw (unresampled, density-weighted) pixels, with the shaded band showing ± 1 standard deviation within the bin; bins containing 20 or fewer pixels are omitted. A curve lying below the 1:1 line indicates under-prediction at that reference level, and a flattening indicates saturation. We repeat the comparison at 10 m (native), 50 m, and 100 m to remove the effect of sub-pixel geolocation error (see Section 5.3) and to show that agreement improves at larger scales; coarser scales are obtained by a moving-window average over the native 10 m grid (5×5 and 10×10 pixels), retaining one aggregated value per native pixel. As shown in Supplementary Figure S10 and Supplementary Figure S11, the binned mean approaches the 1:1 line and the spread narrows at coarser scales.

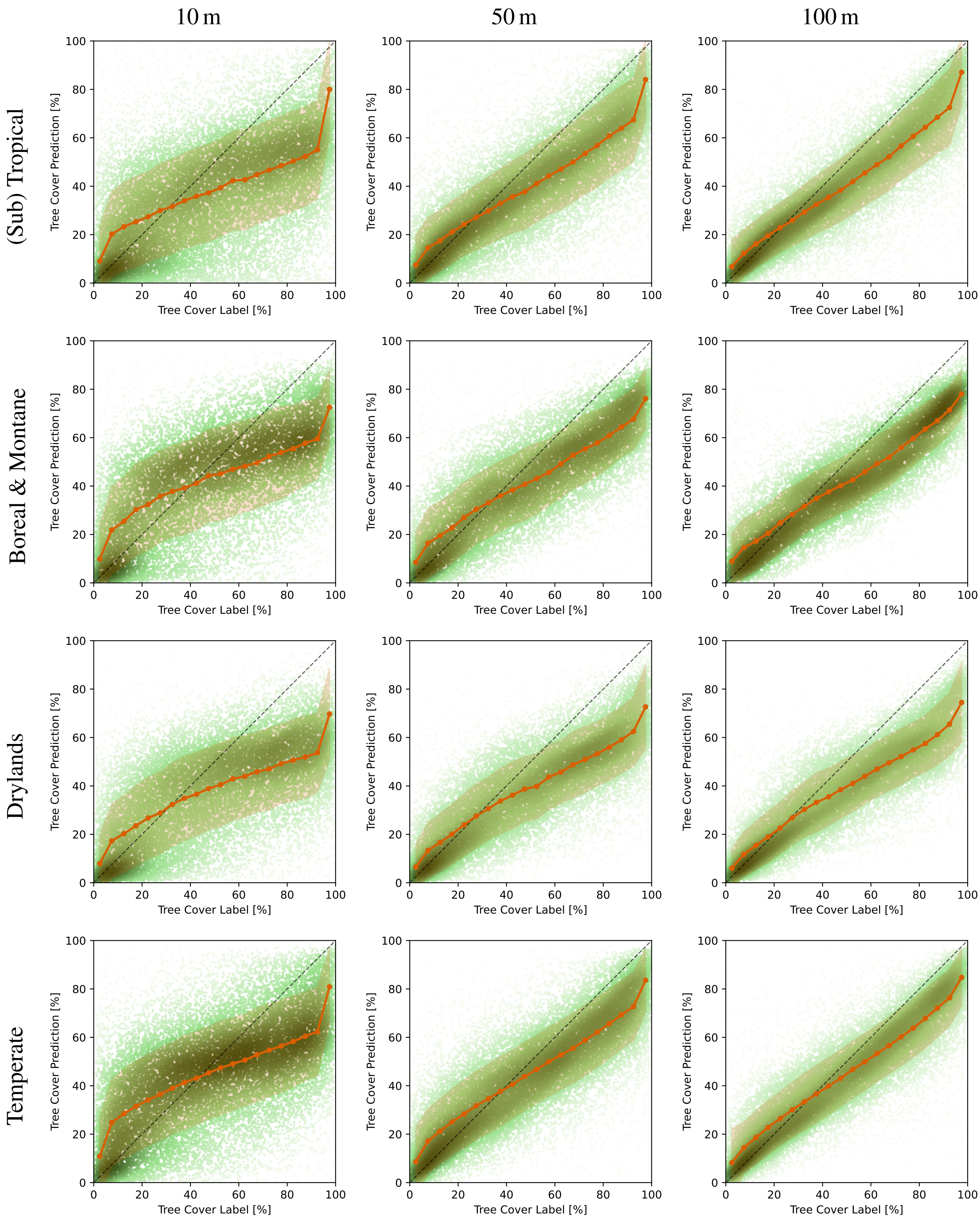

Figure S10: Per-pixel agreement between predicted (y-axis) and drone-derived reference (x-axis) tree cover in percent, by biome (rows) and analysis scale (columns: 10, 50, 100 m), on the held-out test set. Green-to-brown shading shows point density after resampling the reference axis to a uniform marginal; the dashed line is the 1:1 relation, and the orange line with markers is the binned conditional mean (mean prediction per 5% reference-cover bin) with the ± 1 standard deviation band.

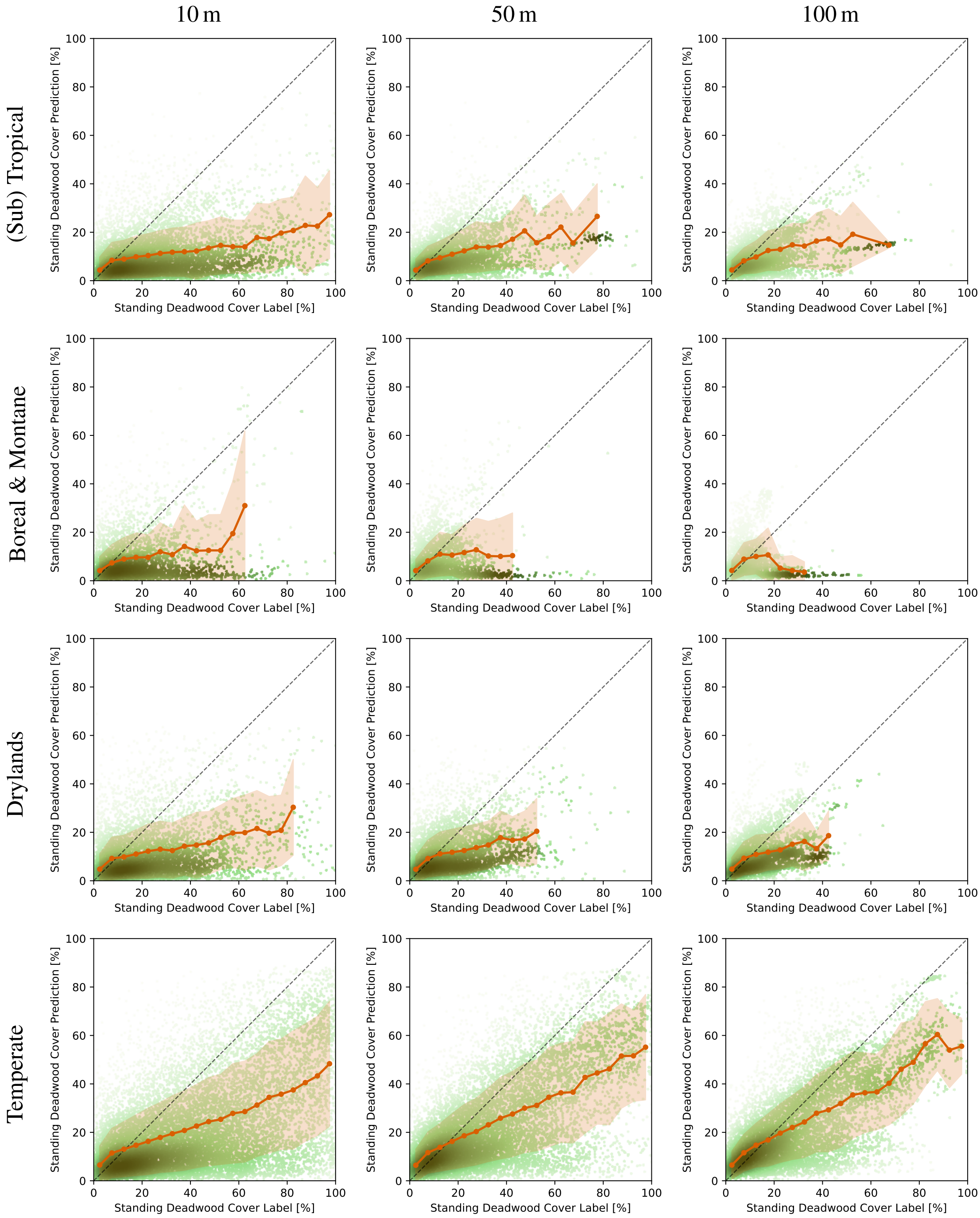

Figure S11: Per-pixel agreement between predicted (y-axis) and drone-derived reference (x-axis) standing deadwood cover in percent, by biome (rows) and analysis scale (columns: 10, 50, 100 m), on the held-out test set. Plotting conventions as in Supplementary Figure S10.

A.8 Recall at higher detection thresholds

The main-text recall (Figure 4) uses an exemplary detection threshold of 10% fractional cover (see Section 2.2.6). For reference, Supplementary Figure S12 shows recall as a function of target cover for the stricter thresholds of 20% and 30%, for tree and standing deadwood cover. As expected, recall decreases at higher thresholds, since a pixel is counted as detected only when the predicted cover exceeds the threshold.

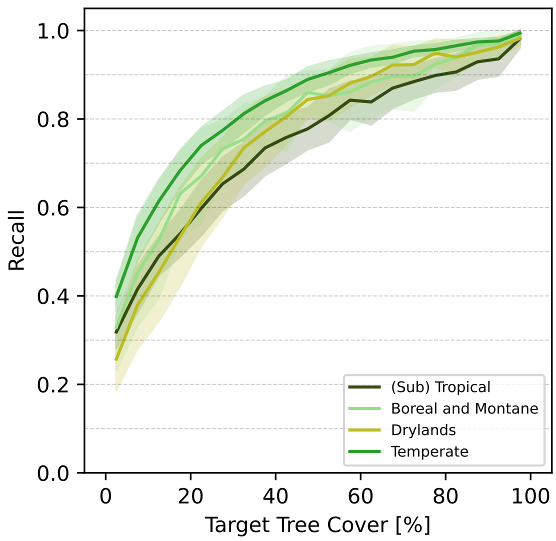

(a) Tree cover, 20% threshold.

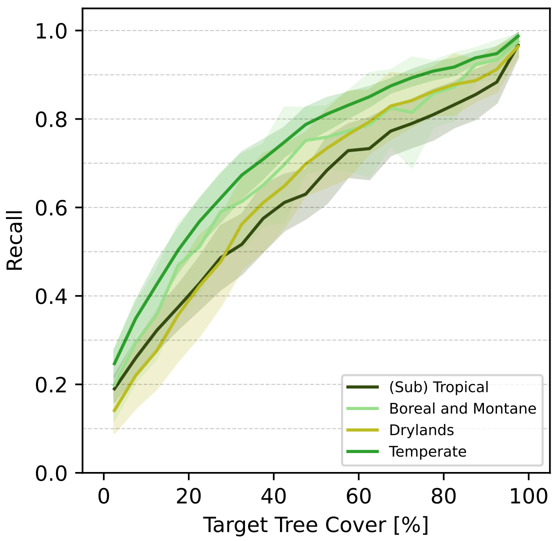

(b) Tree cover, 30% threshold.

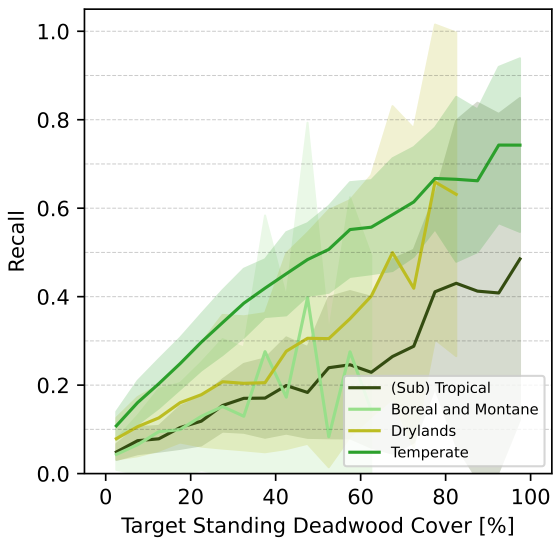

(c) Standing deadwood cover, 20% threshold.

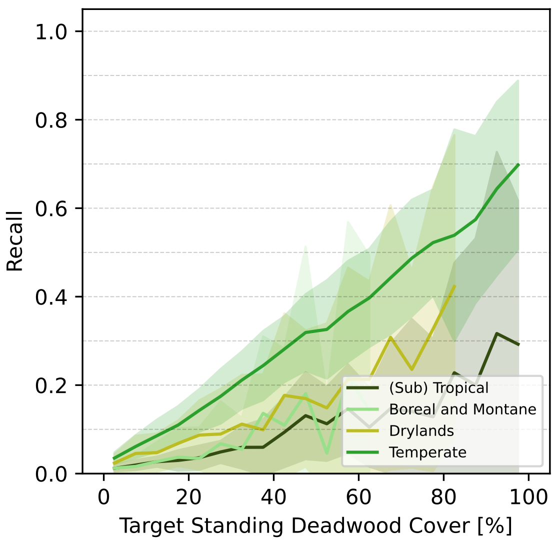

(d) Standing deadwood cover, 30% threshold.

Figure S12: Recall across target fractional cover bins for detection thresholds of 20% and 30% (complementing the 10% threshold used in the main text), per biome. The shaded band shows the minimum-to-maximum range across cross-validation folds.

A.9 Example of multi-year bark beetle outbreak tracking

Supplementary Figure S13 shows how the yearly maps track the multi-year spread of a bark beetle outbreak on the Feldberg, Germany.

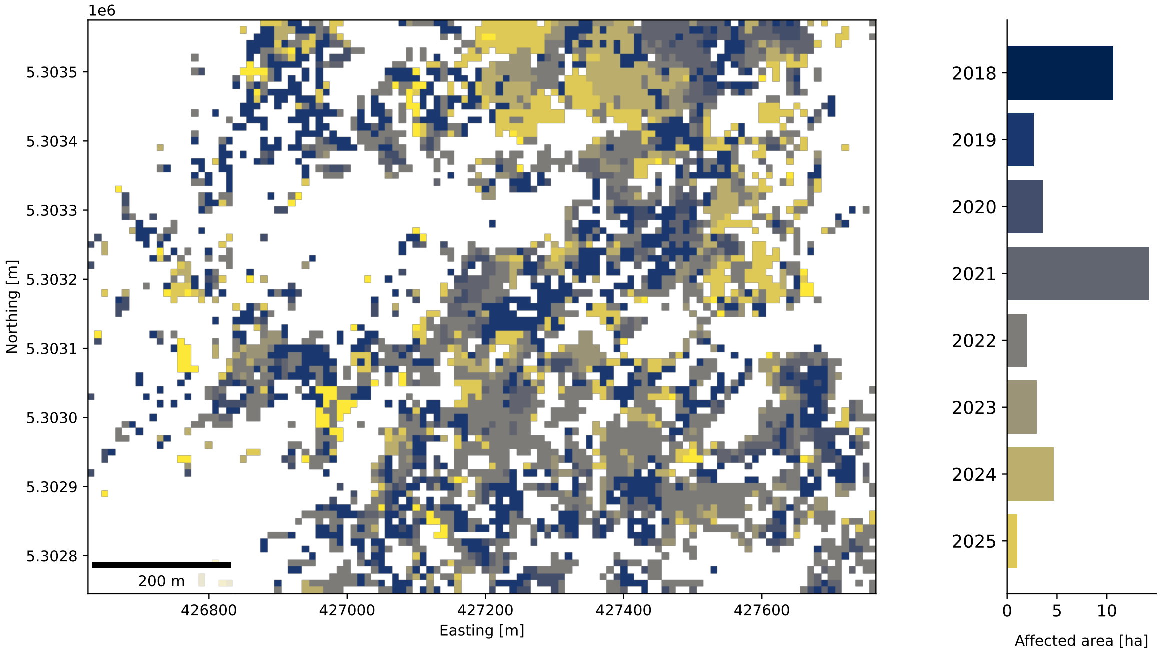

Figure S13: Bark beetle induced mortality spreading from 2018 to 2025 on the Feldberg, Germany (47°52′47.3″N 8°01′01.7″E). Coordinates are in UTM Zone 32N. The color indicates the earliest year where the respective pixel reported above 50% fractional deadwood cover. The barplot on the right displays the number of pixels that were detect first within a specific year.

References

Alix-Garcia, J., & Millimet, D. L. (2023). Remotely incorrect? accounting for nonclassical measurement error in satellite data on deforestation. *Journal of the Association of Environmental and Resource Economists*, *10*(5), 1335–1367.

Allen, C. D., Breshears, D. D., & McDowell, N. G. (2015). On underestimation of global vulnerability to tree mortality and forest die-off from hotter drought in the anthropocene. *Ecosphere*, *6*(8), 1–55.

Anders, T., Hetzer, J., Knapp, N., Forrest, M., Langan, L., Tölle, M. H., Wellbrock, N., & Hickler, T. (2025). Modelling past and future impacts of droughts on tree mortality and carbon storage in norway spruce stands in germany. *Ecological Modelling*, *501*, 110987.

Aybar, C. [Cesar], Ysuhuaylas, L., Loja, J., Gonzales, K., Herrera, F., Bautista, L., Yali, R., Flores, A., Diaz, L., Cuenca, N., et al. (2022). Cloudsen12, a global dataset for semantic understanding of cloud and cloud shadow in sentinel-2. *Scientific data*, *9*(1), 782.

Bauer-Marschallinger, B., & Falkner, K. (2023). Wasting petabytes: A survey of the sentinel-2 utm tiling grid and its spatial overhead. *ISPRS Journal of Photogrammetry and Remote Sensing*, *202*, 682–690.

Beetz, K., Marrs, C., Busse, A., Poděbradská, M., Kinalczyk, D., Kranz, J., & Forkel, M. (2025). Effects of bark beetle disturbance and fuel types on fire radiative power and burn severity in the bohemian-saxon switzerland. *Forestry: An International Journal of Forest Research*, *98*(1), 59–70. https://doi.org/10.1093/forestry/cpae024

Bourgoin, C., Ceccherini, G., Girardello, M., Vancutsem, C., Avitabile, V., Beck, P. S. A., Beuchle, R., Blanc, L., Duveiller, G., Migliavacca, M., Vieilledent, G., Cescatti, A., & Achard, F. (2024). Human degradation of tropical moist forests is greater than previously estimated. *Nature*, *631*(8021), 570–576. https://doi.org/10.1038/s41586-024-07629-0

Bugmann, H., Seidl, R., Hartig, F., Bohn, F., Bruna, J., Cailleret, M., François, L., Heinke, J., Henrot, A.-J., Hickler, T., et al. (2019). Tree mortality submodels drive simulated long-term forest dynamics: Assessing 15 models from the stand to global scale. *Ecosphere*, *10*(2), e02616.

Cheng, Y., Oehmcke, S., Brandt, M., Rosenthal, L., Das, A., Vrieling, A., Saatchi, S., Wagner, F., Mugabowindekwe, M., Verbruggen, W., et al. (2024). Scattered tree death contributes to substantial forest loss in california. *Nature communications*, *15*(1), 641.

Choi, W., Ryu, Y., Kong, J., Jeong, S., & Lee, K. (2025). Evaluation of spatial and temporal variability in sentinel-2 surface reflectance on a rice paddy landscape. *Agricultural and Forest Meteorology*, *363*, 110401.

Copernicus. (n.d.). Level-2a dataset specification. https://sentinels.copernicus.eu/sentinel-data-access/sentinel-products/sentinel-2-data-products/collection-0-level-2a

Copernicus Land Monitoring Service. (2020). Tree cover density.

Coppin, P. R., & Bauer, M. E. (1996). Digital change detection in forest ecosystems with remote sensing imagery. *Remote sensing reviews*, *13*(3-4), 207–234.

D'Andrea, E., Rezaie, N., Battistelli, A., Gavrichkova, O., Kuhlmann, I., Matteucci, G., Moscatello, S., Proietti, S., Scartazza, A., Trumbore, S., et al. (2019). Winter's bite: Beech trees survive complete defoliation due to spring late-frost damage by mobilizing old c reserves. *New Phytologist*, *224*(2), 625–631.

Dick, M. A., Williams, N. M., Bader, M. K.-F., Gardner, J. F., & Bulman, L. S. (2014). Pathogenicity of phytophthora pluvialis to pinus radiata and its relation with red needle cast disease in new zealand. *New Zealand Journal of Forestry Science*, *44*(1), 6.

(ESA), S. (2023, December 11). *Data quality report – sentinel-2 l1c msi, december 2023* (tech. rep. No. Ref. OMPC.CS.DQR.01.11-2023, Issue 94.0). Copernicus Space Component Sentinel Optical Imaging Mission Performance Cluster Service.

Espírito-Santo, F. D., Gloor, M., Keller, M., Malhi, Y., Saatchi, S., Nelson, B., Junior, R. C. O., Pereira, C., Lloyd, J., Frolking, S. [Steve], et al. (2014). Size and frequency of natural forest disturbances and the amazon forest carbon balance. *Nature communications*, *5*(1), 1–6.

European Space Agency. (2021). Copernicus Sentinel-2: Major Products Upgrade Upcoming [Accessed: 2026-01-20].

Farebrother, J., Orbay, J., Vuong, Q., Taïga, A. A., Chebotar, Y., Xiao, T., Irpan, A., Levine, S., Castro, P. S., Faust, A., et al. (2024). Stop regressing: Training value functions via classification for scalable deep rl. *arXiv preprint arXiv:2403.03950*.

Fassnacht, F. E., Mager, C., Waser, L. T., Kanjir, U., Schäfer, J., Buhvald, A. P., Shafeian, E., Schiefer, F., Stančič, L., Immitzer, M., et al. (2025). Forest practitioners' requirements for remote sensing-based canopy height, wood-volume, tree species, and disturbance products. *Forestry: An International Journal of Forest Research*, *98*(2), 233–252.

Frolking, S. [Stephen], Palace, M. W., Clark, D., Chambers, J. Q., Shugart, H., & Hurtt, G. C. (2009). Forest disturbance and recovery: A general review in the context of spaceborne remote sensing of impacts on aboveground biomass and canopy structure. *Journal of Geophysical Research: Biogeosciences*, *114*(G2).

Garbarino, M., Morresi, D., Anselmetto, N., & Weisberg, P. J. (2023). Treeline remote sensing: From tracking treeline shifts to multi-dimensional monitoring of ecotonal change. *Remote Sensing in Ecology and Conservation*, *9*(6), 729–742.

Hammond, W. M., Williams, A. P., Abatzoglou, J. T., Adams, H. D., Klein, T., López, R., Sáenz-Romero, C., Hartmann, H., Breshears, D. D., & Allen, C. D. (2022). Global field observations of tree die-off reveal hotter-drought fingerprint for earth's forests. *Nature Communications*, *13*(1), 1761.

Hansen, M. C. [M. C.], Potapov, P. V., Moore, R., Hancher, M., Turubanova, S. A., Tyukavina, A., Thau, D., Stehman, S. V., Goetz, S. J., Loveland, T. R., Kommareddy, A., Egorov, A., Chini, L., Justice, C. O., & Townshend, J. R. G. (2013). High-resolution global maps of 21st-century forest cover change. *Science*, *342*(6160), 850–853. https://doi.org/10.1126/science.1244693

Hartmann, H., Schuldt, B., Sanders, T. G., Macinnis-Ng, C., Boehmer, H. J., Allen, C. D., Bolte, A., Crowther, T. W., Hansen, M. C. [Matthew C], Medlyn, B. E., et al. (2018). Monitoring global tree mortality patterns and trends. report from the vw symposium 'crossing scales and disciplines to identify global trends of tree mortality as indicators of forest health'. *New Phytologist*, *217*(3), 984–987.

Hartmann, H., Bastos, A., Das, A. J., Esquivel-Muelbert, A., Hammond, W. M., Martínez-Vilalta, J., McDowell, N. G., Powers, J. S., Pugh, T. A., Ruthrof, K. X., et al. (2022). Climate change risks to global forest health: Emergence of unexpected events of elevated tree mortality worldwide. *Annual Review of Plant Biology*, *73*, 673–702.

Hartmann, H., Battisti, A., Brockerhoff, E. G., Bełka, M., Hurling, R., Jactel, H., Oliva, J., Rousselet, J., Terhonen, E., Ylioja, T., et al. (2025). European forests are under increasing pressure from global change-driven invasions and accelerating epidemics by insects and diseases. *Journal für Kulturpflanzen*, *77*(02), 6–24.

Heinken, T., Blumröder, J. S., Adhikari, Y., Balthasar, C., Binder, A., Birkhofer, K., Bischoff, A., Brosinsky, A., Bubner, B., Clerc, D., et al. (2024). Pyrophob-a post-fire ecosystem research project to inform management for resilient forest development. *Tuexenia*, *44*.

Hlásny, T., König, L., Krokene, P., Lindner, M., Montagné-Huck, C., Müller, J., Qin, H., Raffa, K. F., Schelhaas, M.-J., Svoboda, M., et al. (2021). Bark beetle outbreaks in europe: State of knowledge and ways forward for management. *Current Forestry Reports*, *7*(3), 138–165.

Hlásny, T., Perunová, M., Modlinger, R., Blake, M., Brazaitis, G., Csóka, G., de Groot, M., Duduman, M.-L., Faccoli, M., Georgieva, M., et al. (2025). Perspectives: State of national forest damage survey programmes in europe and ways toward improved harmonization and data sharing. *Forest Ecology and Management*, *597*, 123111.

Huete, A., Didan, K., Miura, T., Rodriguez, E. P., Gao, X., & Ferreira, L. G. (2002). Overview of the radiometric and biophysical performance of the modis vegetation indices. *Remote sensing of environment*, *83*(1-2), 195–213.

Imani, E., Luedemann, K., Scholnick-Hughes, S., Elelimy, E., & White, M. (2024). Investigating the histogram loss in regression. *arXiv preprint arXiv:2402.13425*.

Imani, E., & White, M. (2018). Improving regression performance with distributional losses. *International conference on machine learning*, 2157–2166.

International Tree Mortality Network, Senf, C., Esquivel-Muelbert, A., Pugh, T. A., Anderegg, W. R., Anderson-Teixeira, K. J., Arellano, G., Beloiu Schwenke, M., Bentz, B. J., Boehmer, H. J., et al. (2025). Towards a global understanding of tree mortality. *New Phytologist*.

Ioffe, S., & Szegedy, C. (2015). Batch normalization: Accelerating deep network training by reducing internal covariate shift. *Proceedings of the 32nd International Conference on Machine Learning (ICML)*.

Jouy, F., Schüle, M., Adhikari, Y., Binder, A., Clerc, D., Gerwin, W., Heinken, T., Raab, T., Repmann, F., Rönnefarth, S., et al. (2025). Factors impacting the variability of post-fire forest regeneration in central european pine plantations. *Restoration Ecology*, *33*(4), e70017.

Jucker, T., Fischer, F. J., Chave, J., Coomes, D. A., Caspersen, J., Ali, A., Panzou, G. J. L., Feldpausch, T. R., Falster, D., Usoltsev, V. A., Jackson, T. D., Adu-Bredu, S., Alves, L. F., Aminpour, M., Angoboy, I. B., Anten, N. P. R., Antin, C., Askari, Y., Muñoz, R., … Zimmermann, N. E. (2025). The global spectrum of tree crown architecture. *Nature communications*, *16*(1), 4876.

Junttila, S., Blomqvist, M., Laukkanen, V., Heinaro, E., Polvivaara, A., O'Sullivan, H., Yrttimaa, T., Vastaranta, M., & Peltola, H. (2024). Significant increase in forest canopy mortality in boreal forests in southeast finland. *Forest Ecology and Management*, *565*, 122020. https://doi.org/10.1016/j.foreco.2024.122020

Kattenborn, T., Schiefer, F., Frey, J., Feilhauer, H., Mahecha, M. D., & Dormann, C. F. (2022). Spatially autocorrelated training and validation samples inflate performance assessment of convolutional neural networks. *ISPRS Open Journal of Photogrammetry and Remote Sensing*, *5*, 100018.

Khatri-Chhetri, P., van Wagtendonk, L., Hendryx, S. M., & Kane, V. R. (2024). Enhancing individual tree mortality mapping: The impact of models, data modalities, and classification taxonomy. *Remote Sensing of Environment*, *300*, 113914.

Körner, C., Möhl, P., & Hiltbrunner, E. (2023). Four ways to define the growing season. *Ecology Letters*, *26*(8), 1277–1292.

Korznikov, K., Kislov, D., Doležal, J., & Altman, J. (2025). Hidden forest loss: Challenges in detecting wind-and insect-driven forest disturbances with global forest change landsat-based products in mixed southern boreal forests. *Remote Sensing Applications: Society and Environment*, 101798.

Korznikov, K., Kislov, D., Doležal, J., Petrenko, T., & Altman, J. (2022). Tropical cyclones moving into boreal forests: Relationships between disturbance areas and environmental drivers. *Science of the Total Environment*, *844*, 156931.

Liu, S., Brandt, M., Nord-Larsen, T., Chave, J., Reiner, F., Lang, N., Tong, X., Ciais, P., Igel, C., Pascual, A., et al. (2023). The overlooked contribution of trees outside forests to tree cover and woody biomass across europe. *Science Advances*, *9*(37), eadh4097.

Loshchilov, I., & Hutter, F. (2019). Decoupled weight decay regularization. *International Conference on Learning Representations (ICLR)*.

Mahecha, M. D., Gans, F., Brandt, G., Christiansen, R., Cornell, S. E., Fomferra, N., Kraemer, G., Peters, J., Bodesheim, P., Camps-Valls, G., et al. (2020). Earth system data cubes unravel global multivariate dynamics. *Earth System Dynamics*, *11*(1), 201–234.

Meyer, H., & Pebesma, E. (2022). Machine learning-based global maps of ecological variables and the challenge of assessing them. *Nature Communications*, *13*(1), 2208.

Migliavacca, M., Grassi, G., Bastos, A., Cecchirini, G., Ciais, P., Janssens-Maenhout, G., Lugato, E., Mahecha, M. D., Novick, K. A., Peñuelas, J., Pilli, R., Reichstein, M., Avitabile, V., Beck, P. S. A., Barredo, J. L., Forzieri, G., Herold, M., Korosuo, A., Mansuy, N., … Cescatti, A. (2025a). Securing the forest carbon sink for the European Union's climate ambition [Accepted: 28 March 2025; Received: 4 September 2024]. *Nature*. https://doi.org/10.1038/s41586-025-08967-3

Migliavacca, M., Grassi, G., Bastos, A., Ceccherini, G., Ciais, P., Janssens-Maenhout, G., Lugato, E., Mahecha, M. D., Novick, K. A., Peñuelas, J., et al. (2025b). Securing the forest carbon sink for the european union's climate ambition. *Nature*, *643*(8074), 1203–1213.

Mnih, V., & Hinton, G. E. (2012). Learning to label aerial images from noisy data. *Proceedings of the 29th International conference on machine learning (ICML-12)*, 567–574.

Möhring, J., Kattenborn, T., Mahecha, M. D., Cheng, Y., Beloiu Schwenke, M., Cloutier, M., Denter, M., Frey, J., Gassilloud, M., Göritz, A., Hempel, J., Horion, S., Jucker, T., Junttila, S., Khatri-Chhetri, P., Korznikov, K., Kruse, S., Laliberté, E., Maroschek, M., … Mosig, C. (2025). Global, multi-scale standing deadwood segmentation in centimeter-scale aerial images. *ISPRS Open Journal of Photogrammetry and Remote Sensing*, *18*, 100104. https://doi.org/https://doi.org/10.1016/j.ophoto.2025.100104

Montero, D., Mahecha, M. D., Martinuzzi, F., Aybar, C., Klosterhalfen, A., Knohl, A., Anaya, J., Mosig, C., & Wieneke, S. (2025). Transformers vs. recurrent models for estimating forest gross primary production. https://doi.org/10.48550/ARXIV.2511.11880

Montero, D., Mahecha, M. D., Martinuzzi, F., Aybar, C., Klosterhalfen, A., Knohl, A., Koebsch, F., Anaya, J., & Wieneke, S. (2024a). Recurrent neural networks for modelling gross primary production. *IGARSS 2024 - 2024 IEEE International Geoscience and Remote Sensing Symposium*, 4214–4217. https://doi.org/10.1109/igarss53475.2024.10640715

Montero, D., Kraemer, G., Anghelea, A., Aybar, C. [César], Brandt, G., Camps-Valls, G., Cremer, F., Flik, I., Gans, F., Habershon, S., et al. (2024b). Earth system data cubes: Avenues for advancing earth system research. *Environmental Data Science*, *3*, e27.

Mosig, C., Vajna-Jehle, J., Mahecha, M. D., Cheng, Y., Hartmann, H., Montero, D., Junttila, S., Horion, S., Schwenke, M. B., Koontz, M. J., Maulud, K. N. A., Adu-Bredu, S., Al-Halbouni, D., Ali, M., Allen, M., Altman, J., Amorós, L., Angiolini, C., Astrup, R., … Kattenborn, T. (2026). Deadtrees.earth - an open-access and interactive database for centimeter-scale aerial imagery to uncover global tree mortality dynamics. *Remote Sensing of Environment*, *332*, 115027. https://doi.org/https://doi.org/10.1016/j.rse.2025.115027

Nair, V., & Hinton, G. E. (2010). Rectified linear units improve restricted boltzmann machines. *Proceedings of the 27th International Conference on Machine Learning (ICML)*.

Olson, D. M., Dinerstein, E., Wikramanayake, E. D., Burgess, N. D., Powell, G. V. N., Underwood, E. C., D'amico, J. A., Itoua, I., Strand, H. E., Morrison, J. C., Loucks, C. J., Allnutt, T. F., Ricketts, T. H., Kura, Y., Lamoreux, J. F., Wettengel, W. W., Hedao, P., & Kassem, K. R. (2001). Terrestrial Ecoregions of the World: A New Map of Life on Earth: A new global map of terrestrial ecoregions provides an innovative tool for conserving biodiversity. *BioScience*, *51*(11), 933–938. https://doi.org/10.1641/0006-3568(2001)051[0933:TEOTWA]2.0.CO;2

OpenAerialMap Community. (2024). Openaerialmap [Accessed: 2026-01-20].

Park, J. Y., Lichstein, J. W., Muller-Landau, H. C., Wright, S. J., & Bohlman, S. A. (2026). Interspecific variation in leaf phenology and its relationship with plant traits in a seasonal tropical forest. *Functional Ecology*, *40*(2), 433–450.

Pickens, A. H., Hansen, M. C. [Matthew C], Song, Z., Poulson, A., Komarova, A., Baggett, A., Kerr, T., Mikus, A., Ortiz Dominguez, C., Tyukavina, A., et al. (2025). Rapid monitoring of global land change. *Nature Communications*, *16*(1), 8948.

Pietzsch, B. W., Wudel, C., & Berger, U. (2023). Nonparametric upscaling of bark beetle infestations and management from plot to landscape level by combining individual-based with markov chain models. *European Journal of Forest Research*, *142*(1), 129–144. https://doi.org/10.1007/s10342-022-01512-1

Ploton, P., Mortier, F., Réjou-Méchain, M., Barbier, N., Picard, N., Rossi, V., Dormann, C., Cornu, G., Viennois, G., Bayol, N., et al. (2020). Spatial validation reveals poor predictive performance of large-scale ecological mapping models. *Nature communications*, *11*(1), 4540.

Reiche, J., Mullissa, A., Slagter, B., Gou, Y., Tsendbazar, N.-E., Odongo-Braun, C., Vollrath, A., Weisse, M. J., Stolle, F., Pickens, A., et al. (2021). Forest disturbance alerts for the congo basin using sentinel-1. *Environmental Research Letters*, *16*(2), 024005.

Roberts, D. R., Bahn, V., Ciuti, S., Boyce, M. S., Elith, J., Guillera-Arroita, G., Hauenstein, S., Lahoz-Monfort, J. J., Schröder, B., Thuiller, W., et al. (2017). Cross-validation strategies for data with temporal, spatial, hierarchical, or phylogenetic structure. *Ecography*, *40*(8), 913–929.

Rußwurm, M., & Körner, M. (2020). Self-attention for raw optical satellite time series classification. *ISPRS journal of photogrammetry and remote sensing*, *169*, 421–435.

Schiefer, F., Schmidtlein, S., Frick, A., Frey, J., Klinke, R., Zielewska-Büttner, K., Junttila, S., Uhl, A., & Kattenborn, T. (2023). Uav-based reference data for the prediction of fractional cover of standing deadwood from sentinel time series. *ISPRS Open Journal of Photogrammetry and Remote Sensing*, *8*, 100034.

Schiefer, F., Schmidtlein, S., Hartmann, H. H., Schnabel, F., & Kattenborn, T. (2024). Large-scale remote sensing reveals that tree mortality in germany appears to be greater than previously expected. *Under Review*.

Schmehl, M.-T., Adhikari, Y., Balthasar, C., Binder, A., Clerc, D., Dobkowitz, S., Gerwin, W., Günther, K., Hartong, H., Heinken, T., et al. (2025). Monitoring abiotic and biotic parameters of forest regrowth under different management regimes on former wildfire sites in northeastern germany–data from the pyrophob project. *Earth System Science Data*, *17*(11), 6295–6313.

Schmitt, M., Prexl, J., Ebel, P., Liebel, L., & Zhu, X. X. (2020). Weakly supervised semantic segmentation of satellite images for land cover mapping–challenges and opportunities. *arXiv preprint arXiv:2002.08254*.

Schulze, E.-D. (2006). Biological control of the terrestrial carbon sink. *Biogeosciences*, *3*(2), 147–166. https://doi.org/10.5194/bg-3-147-2006

Schwartz, M., Fogel, F., Besic, N., Robert, D., Geist, L., Renaud, J.-P., Monnet, J.-M., Mosig, C., Vega, C., d'Aspremont, A., et al. (2025). Formspot: A decade of tree-level, country-scale forest monitoring. *arXiv preprint arXiv:2512.17021*.

Schwarz, S., Werner, C., Fassnacht, F. E., & Ruehr, N. K. (2024). Forest canopy mortality during the 2018-2020 summer drought years in central europe: The application of a deep learning approach on aerial images across luxembourg. *Forestry: An International Journal of Forest Research*, *97*(3), 376–387.

Senf, C., Pflugmacher, D., Zhiqiang, Y., Sebald, J., Knorn, J., Neumann, M., Hostert, P., & Seidl, R. (2018). Canopy mortality has doubled in europe's temperate forests over the last three decades. *Nature Communications*, *9*(1), 4978.

Senf, C., & Seidl, R. (2021). Mapping the forest disturbance regimes of europe. *Nature Sustainability*, *4*(1), 63–70.

Sexton, J. O., Song, X.-P., Feng, M., Noojipady, P., Anand, A., Huang, C., Kim, D.-H., Collins, K. M., Channan, S., DiMiceli, C., & Townshend, J. R. (2013). Global, 30-m resolution continuous fields of tree cover: Landsat-based rescaling of modis vegetation continuous fields with lidar-based estimates of error. *International Journal of Digital Earth*, *6*(5), 427–448. https://doi.org/10.1080/17538947.2013.786146

Silvestro, R., Rossi, S., Berthiaume, R., Bauce, É., Rademacher, T., & Deslauriers, A. (2025). The impact of forest tent caterpillar defoliation on maple fitness and syrup production. *Forest Ecology and Management*, *595*, 123011.

Sitch, S., Huntingford, C., Gedney, N., Levy, P., Lomas, M., Piao, S., Betts, R., Ciais, P., Cox, P., Friedlingstein, P., et al. (2008). Evaluation of the terrestrial carbon cycle, future plant geography and climate-carbon cycle feedbacks using five dynamic global vegetation models (dgvms). *Global change biology*, *14*(9), 2015–2039.

Söchting, M., Scheuermann, G., Montero, D., & Mahecha, M. D. (2025). Interactive earth system data cube visualization in jupyter notebooks. *Big Earth Data*, *9*(2), 321–335.

Song, Z., Hansen, M., Pickens, A. H., Poulson, A. J., Baggett, A., Komarova, A., Lima, A., Mikus, A., Ortiz Dominguez, C., & Kerr, T. (2024). Dist-alert: Near-real time monitoring system of land cover change. *AGU Fall Meeting Abstracts*, *2024*, GC41B–02.

Trumbore, S., Brando, P., & Hartmann, H. (2015). Forest health and global change. *Science*, *349*(6250), 814–818.

Tseng, G., Cartuyvels, R., Zvonkov, I., Purohit, M., Rolnick, D., & Kerner, H. (2023). Lightweight, pre-trained transformers for remote sensing timeseries. *arXiv preprint arXiv:2304.14065*.

U.S. Forest Service. (2025). Insect and disease survey (ids) — forest health protection [Accessed via Ïnsect & Disease Explorerät USDA LCMS; data publicly available under Creative Commons Attribution license]. https://apps.fs.usda.gov/lcms-viewer/IDS.html

van der Woude, S., Reiche, J., Balling, J., Nabuurs, G.-J., Sterck, F., Welsink, A.-J., Slagter, B., & Herold, M. (2026). European forest disturbance alerting using sentinel-1. *Remote Sensing of Environment*, *337*, 115325.

Vancutsem, C., Achard, F., Pekel, J.-F., Vieilledent, G., Carboni, S., Simonetti, D., Gallego, J., Aragao, L. E., & Nasi, R. (2021). Long-term (1990–2019) monitoring of forest cover changes in the humid tropics. *Science advances*, *7*(10), eabe1603.

Veitch-Michaelis, J., Cottam, A., Schweizer, D., Broadbent, E., Dao, D., Zhang, C., Almeyda Zambrano, A., & Max, S. (2024). Oam-tcd: A globally diverse dataset of high-resolution tree cover maps. In A. Globerson, L. Mackey, D. Belgrave, A. Fan, U. Paquet, J. Tomczak, & C. Zhang (Eds.), *Advances in neural information processing systems* (pp. 49749–49767, Vol. 37). Curran Associates, Inc. https://proceedings.neurips.cc/paper_files/paper/2024/file/58efdd77196fa8159062afa0408245da-Paper-Datasets_and_Benchmarks_Track.pdf

Viana-Soto, A., & Senf, C. (2025). The european forest disturbance atlas: A forest disturbance monitoring system using the landsat archive. *Earth System Science Data*, *17*(6), 2373–2404.

Watt, M. S., Holdaway, A., Watt, P., Pearse, G. D., Palmer, M. E., Steer, B. S. C., Camarretta, N., McLay, E., & Fraser, S. (2024). Early prediction of regional red needle cast outbreaks using climatic data trends and satellite-derived observations. *Remote Sensing*, *16*(8). https://doi.org/10.3390/rs16081401

White, J. C., Wulder, M. A., Hermosilla, T., Coops, N. C., & Hobart, G. W. (2017). A nationwide annual characterization of 25 years of forest disturbance and recovery for canada using landsat time series. *Remote Sensing of Environment*, *194*, 303–321.

Wijas, B. J., Allison, S. D., Austin, A. T., Cornwell, W. K., Cornelissen, J. H. C., Eggleton, P., Fraver, S., Ooi, M. K., Powell, J. R., Woodall, C. W., et al. (2024). The role of deadwood in the carbon cycle: Implications for models, forest management, and future climates. *Annual Review of Ecology, Evolution, and Systematics*, *55*.

Winter, C., Mueller, S., Kattenborn, T., Stahl, K., Szillat, K., Weiler, M., & Schnabel, F. (2024). Forest dieback in drinking water protection areas–a hidden threat to water quality. *bioRxiv*, 2024–08.

Xu, Y., Ciais, P., Santoro, M., Bourgoin, C., Ritter, F., Pellissier-Tanon, A., Feng, Y., Zhou, C., He, G., Heinrich, V., Besnard, S., Robinson, N., Cook-Patton, S. C., Chave, J., Aragao, L. E. O. C., Ometto, J. P., Bowring, S. P. K., Fayad, I., Zhu, L., … Li, W. (2026). Small persistent humid forest clearings drive tropical forest biomass losses. *Nature*, *649*(8096), 375–380. https://doi.org/10.1038/s41586-025-09870-7

Yan, Y., Piao, S., Hammond, W. M., Chen, A., Hong, S., Xu, H., Munson, S. M., Myneni, R. B., & Allen, C. D. (2024). Climate-induced tree-mortality pulses are obscured by broad-scale and long-term greening. *Nature Ecology & Evolution*, *8*(5), 912–923.

Yuan, Y., Lin, L., Liu, Q., Hang, R., & Zhou, Z.-G. (2022). Sits-former: A pre-trained spatio-spectral-temporal representation model for sentinel-2 time series classification. *International Journal of Applied Earth Observation and Geoinformation*, *106*, 102651.

Zanaga, D., Van De Kerchove, R., Daems, D., De Keersmaecker, W., Brockmann, C., Kirches, G., Wevers, J., Cartus, O., Santoro, M., Fritz, S., Lesiv, M., Herold, M., Tsendbazar, N., Xu, P., Ramoino, F., & Arino, O. (2022). ESA WorldCover 10 m 2021 v200. https://doi.org/10.5281/zenodo.7254221

Zhang, H. K., Camps-Valls, G., Liang, S., Tuia, D., Pelletier, C., & Zhu, Z. (2025). Preface: Advancing deep learning for remote sensing time series data analysis.

Zhang, X., Friedl, M., & Henebry, G. (2020). VIIRS/NPP Land Cover Dynamics Yearly L3 Global 500m SIN Grid V001 [[Data set]]. https://doi.org/10.5067/VIIRS/VNP22Q2.001

Zhang, Y., Ling, F., Wang, X., Foody, G. M., Boyd, D. S., Li, X., Du, Y., & Atkinson, P. M. (2021). Tracking small-scale tropical forest disturbances: Fusing the landsat and sentinel-2 data record. *Remote Sensing of Environment*, *261*, 112470.

Zhou, Q., Neigh, C. S., Ju, J., Dabney, P., Cook, B., Zhu, Z., Crawford, C. J., Gascon, F., Strobl, P., & Sridhar, M. (2025). Towards seamless global 30-meter terrestrial monitoring: Evaluating 2022 cloud free coverage of harmonized landsat and sentinel-2 (hls) v2. 0. *IEEE Geoscience and Remote Sensing Letters*.

Zhu, Z., Wang, S., & Woodcock, C. E. (2015). Improvement and expansion of the fmask algorithm: Cloud, cloud shadow, and snow detection for landsats 4–7, 8, and sentinel 2 images. *Remote sensing of Environment*, *159*, 269–277.

Zhu, Z., & Woodcock, C. E. (2012). Object-based cloud and cloud shadow detection in landsat imagery. *Remote sensing of environment*, *118*, 83–94.